

IMPERIAL

DEPARTMENT OF EARTH SCIENCE AND ENGINEERING

IMPERIAL COLLEGE LONDON

Impact of Late Neogene Dynamic Topography on Antarctic and Greenland Ice-Sheet Stability

Author:

Luke Broadley

Supervisor:

Dr Fred Richards

Date: January 7, 2025

This report is submitted as part requirement for the MSci degree in Geophysics at Imperial College London. It is substantially the result of my own work except where indicated explicitly in the text. The report may be freely copied and distributed provided the source is acknowledged explicitly.

Abstract

Ice-sheet models that underpin current projections of future sea-level change are often calibrated using palaeo-ice volume estimates for the Mid-Pliocene Warm Period (MPWP; ~ 3 Ma), the most recent interval with climatic conditions approximating those expected in the near future. Bedrock topography is a major control on ice-sheet volumes predicted by these models, since marine-based regions are highly susceptible to runaway destabilisation, and they currently assume that MPWP bedrock topography was the same as at present. However, dynamic topography (DT; i.e., topography supported by convectively generated stresses) is likely to have evolved substantially over the past ~ 3 Ma, invalidating this assumption. No study has yet assessed this impact on Greenland's MPWP equilibrium ice volume, while only one study has done so for the Antarctic Ice Sheet (AIS) using relatively low-resolution seismic tomography to predict mantle flow patterns. This study aims to more accurately quantify DT impacts on Pliocene ice-sheet stability at both poles using high-resolution seismic tomographic and geodynamic models. Existing DT predictions and observations are compared, finding generally good agreement, though a +0.8 km offset in observed values is seen in Greenland. This feature can be explained by invoking isostatic elevation of melt-depleted oceanic mantle lithosphere resulting from Iceland-plume–mid-ocean-ridge interaction. Improved correlations motivate incorporation of a higher-resolution Antarctic mantle model into DT predictions by merging it in temperature space with a lower resolution global model. The resulting mantle convection simulations and reconstructions of post-MPWP DT change enable more accurate prediction of Pliocene bedrock topography. Ice-sheet models run on both DT-corrected MPWP topography and present-day topography show differences in steady-state ice volume of ~ 1.8 m sea-level equivalent (SLE), with complete loss of the Ross Ice Shelf occurring in the former. This substantial DT-related component of observed MPWP sea-level excess suggests existing estimates of climatically controlled AIS contributions need to be lowered, reducing inferred ice-sheet sensitivity. Recalibrating existing sea-level projections accordingly reduces predicted end-of-century Antarctic contributions to future sea level change by 45%.

This project began on the 1st October 2024 and concluded on the 7th January 2025. No summer work was undertaken.

Word Count: 5477

Contents

1	Introduction	4
2	Comparing Observations and Predictions of Polar Present-Day Dynamic Topography	6
2.1	Methodology and Data	6
2.1.1	Comparing Existing Models	6
2.1.2	Isostatic Balance	6
2.1.3	Residual Velocity Comparison	9
2.2	Results	9
2.2.1	Comparing Existing Models	9
2.2.2	Isostatic Balance	9
2.2.3	Residual Velocity Comparison	9
2.3	Discussion	13
3	Temperature, Convection and Dynamic Topography Models	13
3.1	Methodology	13
3.1.1	Model Merge	14
3.1.2	Convection and Dynamic Topography Models	14
3.2	Results	16
3.3	Discussion	20
4	Palaetopography and Ice-sheet Models	21
4.1	Methodology	21
4.2	Results	22
4.3	Discussion	24
5	Conclusions	27
A	Appendices	32
A.1	Appendix A: Detailed Methods / Discussion	32
A.1.1	Antarctic DT-RT Mismatch	32
A.1.2	Temperature Models Merging Methodology	32
A.1.3	Merged Model Present-day Dynamic Topography	35
A.2	Appendix B: Extra Models	35
A.2.1	Extra Dynamic Topography and Residual Topography Datasets	35
A.2.2	Extra Ice Sheet Models	35

List of Figures

1	Bedrock Topography	5
2	Isostatic Balance	7
3	Dynamic Topography : Residual Topography Correlation	8
4	Depleted Lithosphere Density Offsets and Thicknesses	10
5	Residual Vs : Residual Topography Antarctica Correlation Heatmaps	11
6	Residual Vs : Residual Topography Greenland Correlation Heatmaps	12
7	Temperature Models and Neogene-Quaternary Magmatism	14
8	Temperature Model Merging Methods	15
9	ASPECT Input Temperature Depth Slices	17
10	Antarctica Convection Model	18
11	Greenland Convection Model	19
12	Antarctica Dynamic Topography Change Since 3Ma	20
13	Greenland Dynamic Topography Change Since 3Ma	21
14	Palaeotopography	23
15	Antarctica Ice Type	24
16	Antarctica Ice Thickness	25
17	Greenland Ice Thickness	26
18	Future Sea-level Rise Predictions	27
19	Merged and SLNAAFSA Present-day Dynamic Topography Models ($\pm 45^{\circ}\text{S}$)	33
20	Merged and SLNAAFSA Present-day Dynamic Topography Models	34
21	Dynamic Topography : Residual Topography Correlation (Extra Models)	36
22	Antarctica Ice Thicknesses (Extra Models)	38
23	Greenland Ice Thicknesses (Extra Models)	39
24	Antarctic Ice Volume Timeseries	40
25	Greenland Ice Volume Timeseries	41

List of Tables

1	Isostasy Balance Results	9
---	------------------------------------	---

1 Introduction

Predicting future ice-sheet behaviour and subsequent sea-level change requires accurate modelling of present and past ice-sheets ([Paxman, 2023](#)). Models are often run under Mid-Pliocene Warm Period (MPWP) climatic conditions, ~3 Ma, as they were relatively similar to those expected in the near future, with ~400 ppm of CO₂ and temperatures ~2.0 - 3.5 °C higher than pre-industrial temperatures ([DeConto et al., 2021](#)). By excluding model parameterisations inconsistent with MPWP global mean sea-level estimates, the response of modern ice-sheets to future climate change can be more confidently predicted, helping to reduce uncertainty in sea-level projections ([Richards et al., 2023a](#)).

Ice-sheet areas particularly susceptible to retreat, therefore critical in modelling, are marine-based ice sheets, where ice is grounded underwater. These are subjected to warmer ocean temperatures, and are at the risk of runaway processes like Marine Ice Sheet Instability (MISI). This is proposed to occur when bedrock slopes downwards inland from the grounding line, meaning the surface area of ice exposed to warm seawater grows as the ice-sheet margin retreats, causing ever-increasing rates of melting and retreat. The Marine Ice Cliff Instability (MICI) may also significantly impact the stability of marine-based ice-sheets that are unbuttressed and bounded by ice cliffs over a critical height, however this process is not as clearly understood ([DeConto et al., 2021; Paxman, 2023; Richards et al., 2023a](#)). Bedrock topography is therefore a major control on ice-sheet stability, and accurate constraint on this is essential for producing reliable ice-sheet models ([Austermann et al., 2015](#)).

The majority of West Antarctica (WA) sits below sea-level, with most of the West Antarctic ice-sheet (WAIS) being marine-based (Figure 1). More of the East Antarctic ice-sheet (EAIS) is land-based, though there are large basins, e.g. Wilkes Basin and Aurora Basin, that sit below sea-level, being marine-based at their grounding lines ([Mitrovica et al., 2020](#)). Overall, ~45% of the AIS is currently grounded below sea-level ([Paxman et al., 2020](#)). Unloading the AIS makes East Antarctica (EA) significantly more land-based, whilst WA remains mostly marine-based, indicating West Antarctica is the area most at risk of collapse. Greenland has higher topography at the coastlines (Figure 1), meaning the Greenland ice-sheet (GIS) is less likely to be marine based at its' grounding lines, though marine-based outlets do exist, like Jakobshavn Glacier ([DeConto et al., 2021](#)). Unloading of the GIS primarily appears to raise inland Greenland above sea-level.

Uncertainty in ice-sheet-model-based sea-level projections can be reduced by tuning model instability parameters to reproduce ice loss consistent with MPWP GMSL estimates ([DeConto et al., 2021](#)). While these model runs account for differences in climate, they assume MPWP bedrock topography is equal to present, ignoring the potentially significant impact of dynamic topography (DT). Mantle convective processes, driven by thermal and compositional density anomalies, exert normal stresses on the base of the lithosphere, creating uplift or subsidence ([Mitrovica et al., 2020](#)). This may influence ice-sheet stability over time, and therefore equilibrium ice-sheet volumes, particularly where grounding-lines move above or below sea-level. Present-day DT, measured by proxy by correcting topography for isostatic and flexural effects, as well subsidence due to cooling of oceanic lithosphere with age e.g. [Hoggard et al. \(2017\)](#); [Holdt et al. \(2022\)](#), show amplitudes can reach up to ~2 km, with significant impact over relatively short wavelengths (~1000 km). Key ice-sheet model parameters in existing studies may therefore be miscalibrated, damaging the reliability of sea-level projections, with [Richards et al. \(2023a\)](#) showing DT can have significant impacts over recent, relevant timescales.

No study has directly assessed the effect of DT change on Greenland's MPWP equilibrium ice volume and, although one study has attempted this for Antarctica, its mantle flow predictions are based on a seismic tomographic model with limited resolution at wavelengths <2500 km(i.e., spherical harmonic degree, $l > 16$) [Simmons et al., 2009](#)). Here, I aim to rem-

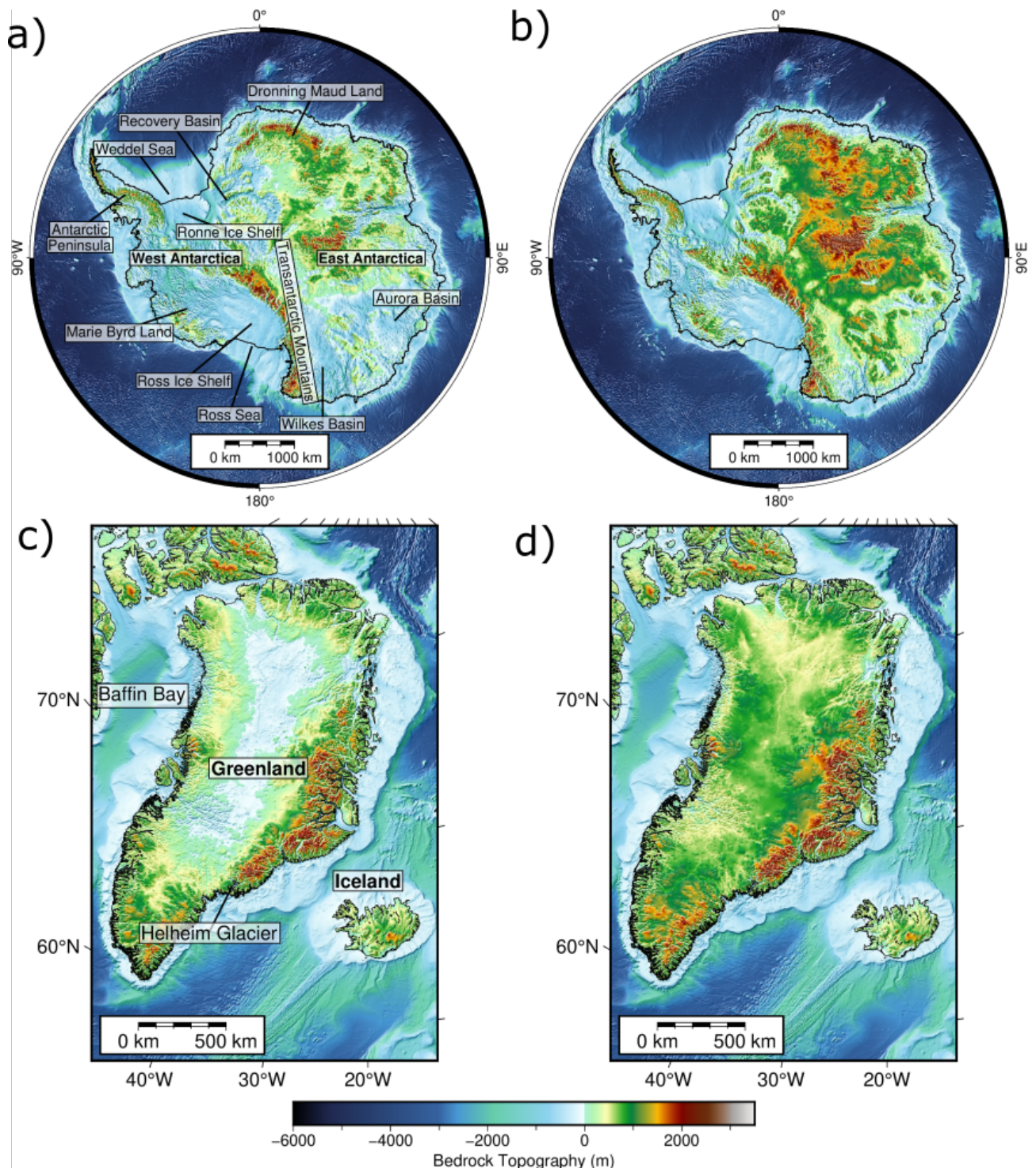


Figure 1: Bedrock topography maps of Antarctica and Greenland. a) and b) show current bedrock topography for Antarctica and Greenland respectively, from [NOAA National Centers for Environmental Information \(2022\)](#). c) and d) show the same ETOPO bedrock with the respective ice sheets isostatically unloaded, using isostatic correction data from [Paxman et al. \(2022\)](#). All maps use the colour palette indicated by the bottom colour scale.

edy this situation using recent, high-resolution seismic tomographic models ([Lloyd et al., 2020](#); [Celli et al., 2021](#); [Schaeffer and Lebedev, 2013](#)) and geodynamic datasets ([Hoggard et al., 2017](#); [Holdt et al., 2022](#)) to more accurately quantify the change in DT's contribution to reduced polar ice volumes and higher GMSL observed during the MPWP. First, existing present-day DT datasets are analysed and compared with seismic tomographic models to determine which upper mantle velocity structure correlates best with observed surface deflections. Next, optimal tomographic models are used to simulate the spatio-temporal evolution of global mantle flow, and associated DT changes, since the MPWP. Finally, by subtracting predicted DT changes from modern datasets, MPWP subglacial bedrock topography is reconstructed and incorporated into ice-sheet models to quantify the impact of post-Pliocene DT change on equilibrium ice volumes and equivalent GMSL. These results are used to revise estimates of AIS contributions to MPWP GMSL and quantify the impact of previously neglected post-Pliocene DT changes on existing sea-level projections.

2 Comparing Observations and Predictions of Polar Present-Day Dynamic Topography

2.1 Methodology and Data

2.1.1 Comparing Existing Models

Residual topography measurements (RT; [Hoggard et al., 2017](#); [Holdt et al., 2022](#)) were first compared with existing model predictions of present-day dynamic topography (DT; [Richards et al., 2023b](#)).

The RT datasets are both constructed using modern oceanic seismic reflection and refraction profiles, plate cooling models, and geodetic observations to correct seafloor bathymetry for isostatic deflections resulting from crustal and sedimentary thickness variations, age-dependent lithospheric cooling, and geoid height anomalies. The principal difference is that [Holdt et al. \(2022\)](#) substantially expands the [Hoggard et al. \(2017\)](#) RT compilation by including older seismic datasets. Only oceanic RT data is used here, as it is more readily available than continental data, owing to complications with continental heterogeneities ([Hoggard et al., 2017](#)).

The present-day DT model calculates instantaneous mantle flow models and associated DT using sensitivity kernels. The model predictions adopt upper mantle density anomalies inferred from a calibrated anelastic parameterisation of the SLNAAFSA seismic tomographic model [Richards et al. \(2020\)](#); [Hoggard et al. \(2020a\)](#), while lower mantle density anomalies are determined from five different seismic tomographic models, using thermodynamic calculations to predict the V_S - density relationship for a given mantle composition ([Richards et al., 2023b](#)). For each, the chemical structure of large-low velocity provinces (LLVPs) is optimised to fit current geodynamic observables when each density model is combined with one of three radial viscosity models. The 15 resulting outputs are averaged here into a single model.

RT points were plotted over DT models to highlight similarities and discrepancies. Since DT predictions are calculated up to a maximum spherical harmonic degree, $l_{\max} = 30$, RT values are sampled from their $l = 1\text{--}30$ spherical harmonic expansions, ensuring direct comparability. After extracting RT and DT values at RT data locations, linear regression was performed to determine correlations and best-fit lines.

2.1.2 Isostatic Balance

Best-fitting RT-DT linear relationships obtained for Greenland and Antarctica are offset by 0.8 ± 0.2 km for both RT datasets. This result could reflect the influence of the Iceland plume

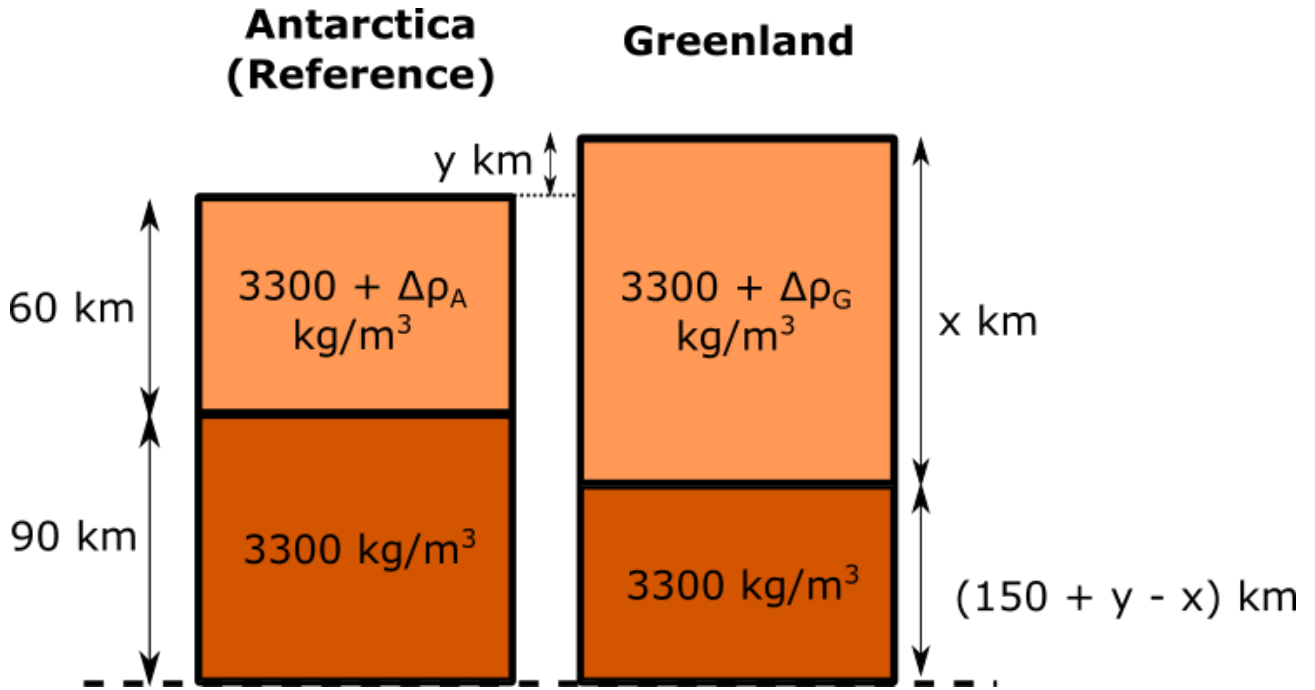


Figure 2: Cartoon of isostatic balance. Values inside boxes are densities, with $\Delta\rho_A$ and $\Delta\rho_G$ representing density offsets of the depleted mantles of Antarctica and Greenland. Values on the sides represent thicknesses, with a reference thickness of 60 km in Antarctica and x representing the thickness of the depleted lithosphere in Greenland. y represents the amount of RT offset, determined from the central, maximum and minimum separations of their best-fit RT-DT relationships. Dashed line is compensation depth for a column thickness of 150 km.

on thermochemical structure of North Atlantic oceanic lithosphere, since elevated temperatures would have triggered deeper, higher-volume melting at the mid-ocean ridge over at least the Cenozoic Era. This greater extent of melting would create a thicker layer of low-density depleted mantle, impacting the mean oceanic elevation of the two regions ([Shorttle et al., 2014](#); [Celli et al., 2021](#)). This is tested with an isostatic balance.

Reference column values are displayed in Figure 2. A reference density offset of $\Delta\rho_A = -23$ kg/m³ is obtained for ambient mantle potential temperature (1300 °C) using the melting parameterisation of [Shorttle et al. \(2014\)](#).

RT has already been corrected for isostatic topography changes caused by crustal thickness variations, so the crust can be ignored in these calculations. Pressures at the base of each rock column were balanced with the following equation:

$$60(3300 + \Delta\rho_A) + 90(3300) = (150 + y - x)(3300) + x(3300 + \Delta\rho_G) \quad (1)$$

simplifying to the following when substituting $\Delta\rho_A$:

$$\Delta\rho_G = -\frac{C}{x} \quad (2)$$

where C is a function of RT offset. The [Shorttle et al. \(2014\)](#) melting parameterisation was used to calculate layer thicknesses and average density offsets for sub-ridge depleted mantle at 1300–1600 °C mantle potential temperatures (T_P ; Figure 4). Predicted T_P at the intersection between the resulting density versus depleted layer thickness relationship and that of the isostatic balance (Eqn 2) is then compared with independent petrological estimates of present-day mantle T_P beneath Iceland.

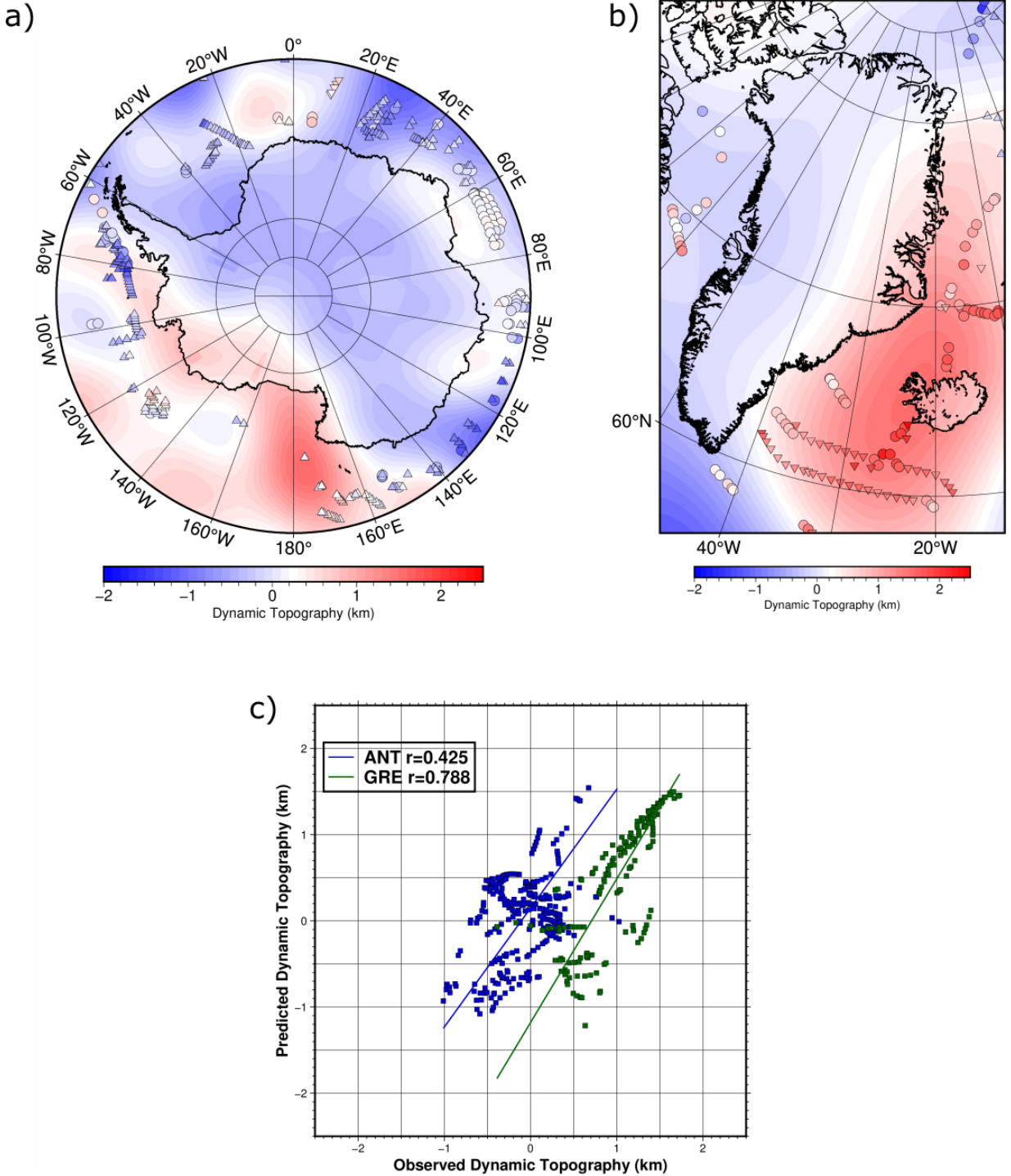


Figure 3: a), b) Map of Antarctica, Greenland respectively. Grid data is predicted present-day DT from *Richards et al.* (2023b). Point data (circles, triangles) are RT measurements from *Hoggard et al.* (2017). Circles represent data-points corrected for both sediment and crustal thickness, triangles only corrected for sediment thickness, representing upper and lower bounds, following the symbol style of *Hoggard et al.* (2017). Both the residual and dynamic topography data are plotted with the same colour-scheme. c) Plot of model dynamic topography vs observed residual topography. Antarctic data points in blue, Greenland data points in green, with Pearson's correlation coefficient, r , displayed in legend.

Data Offset (km)	Thickness (km)	Density Offset (kg/m^3)	Potential Temperature ($^\circ\text{C}$)
0.6	93.7	-35.5	~ 1450
0.8	104.1	-38.6	~ 1485
1.0	114.2	-40.8	~ 1518

Table 1: Thickness, density offset and associated mantle potential temperature, from [Shorttle et al. \(2014\)](#), of the depleted lithosphere layer in Greenland.

2.1.3 Residual Velocity Comparison

RT was also compared to a set of upper-mantle seismic tomographic models to investigate correlations and determine the most suitable dataset for mantle convection modelling. Datasets considered were: SLNAAFSA ([Hoggard et al., 2016](#); [Richards et al., 2020](#)), a global vertically polarised shear wave (V_{SV}) model; NAT2021 [Celli et al. \(2021\)](#), a V_{SV} model for the North Atlantic; and ANT-20 ([Lloyd et al., 2020](#)), a full-waveform radially anisotropic model for Antarctica. All models cover the upper mantle and transition zone.

To enable comparison with RT datasets, oceanic ‘residual’ V_S was calculated by removing trends associated oceanic lithospheric cooling via subtraction of average V_S as a function of age from each depth slice in the model (see [Richards et al., 2020](#)). V_{SV} was used for SLNAAFSA and NAT2021, while the Voigt average V_S is used for ANT-20. Residual V_S data was stacked and averaged over a range of depth extents, varying top and bottom stacking depths between 25 and 400 km. Mean residual V_S was then extracted from each stack at the locations of RT points, and correlation coefficients were calculated. Heatmaps were generated, Figures 5 6, to summarise changes in correlations as a function of stacking depth bounds.

2.2 Results

2.2.1 Comparing Existing Models

Predicted DT generally correlates well with RT observations (Figure 3) and their magnitudes are broadly similar. However, agreement is notably poorer in two locations. Baffin Bay is predicted to have negative DT but RT measurements indicate a positive anomaly, while positive DT and negative RT characterise the Amundsen Sea region of WA.

Overall, Greenland’s RT data agrees better with predictions than Antarctica’s, which is consistent across other models in Appendix A.2.1. Lower correlations in Antarctica suggest the need for more accurate RT and tomographic datasets in this region, though SLNAAFSA is seemingly appropriate for Greenland.

2.2.2 Isostatic Balance

Isostatic balance calculations show the Greenland RT offset is consistent with a 104 km depleted layer thickness, and a density offset of -38.6 kg/m^3 (Figure 4, Table 1). These values correspond to a T_P of $\sim 1485^{+33}_{-35} \text{ }^\circ\text{C}$, which aligns remarkably well with petrological estimates of Iceland plume excess T_P ([Matthews et al., 2016](#), $1480^{+37}_{-30} \text{ }^\circ\text{C}$). This result strongly suggests that the observed RT offset stems from anomalous depletion of the North Atlantic oceanic lithosphere caused by sustained interaction of the Iceland plume with regional MORs.

2.2.3 Residual Velocity Comparison

For Antarctica, SLNAAFSA best fits RT data with deep stacking depths, around 300 km (Figure 5), ranging 300–325 km at best which, given a 25 km depth resolution, only covers 2

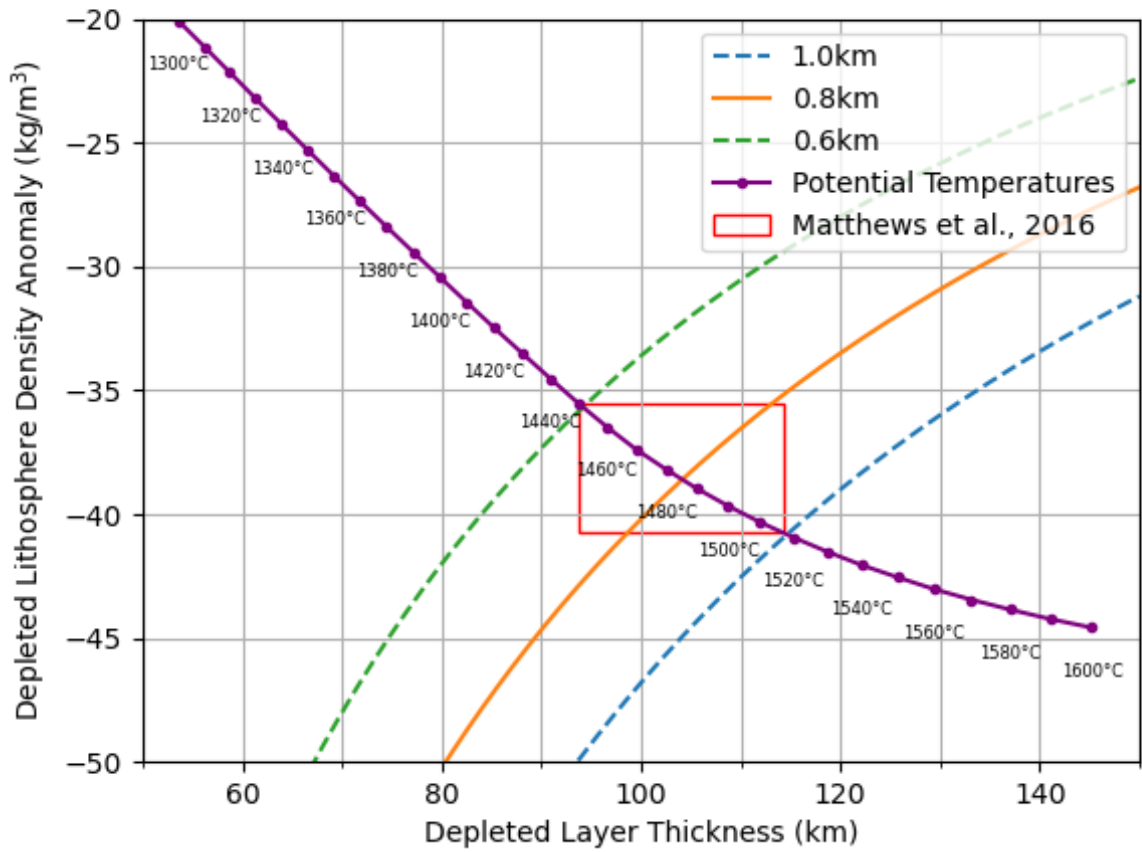


Figure 4: Depleted lithosphere thickness against density anomaly. Green, orange and blue lines represent sets of solutions for the isostatic balance with assumed data offsets listed in the legend. Purple line represents expected values for a range of mantle potential temperatures, increasing 10°C every data-point, from *Shorttle et al.* (2014). Red box represents range of expected potential temperatures for the Iceland plume found in *Matthews et al.* (2016).

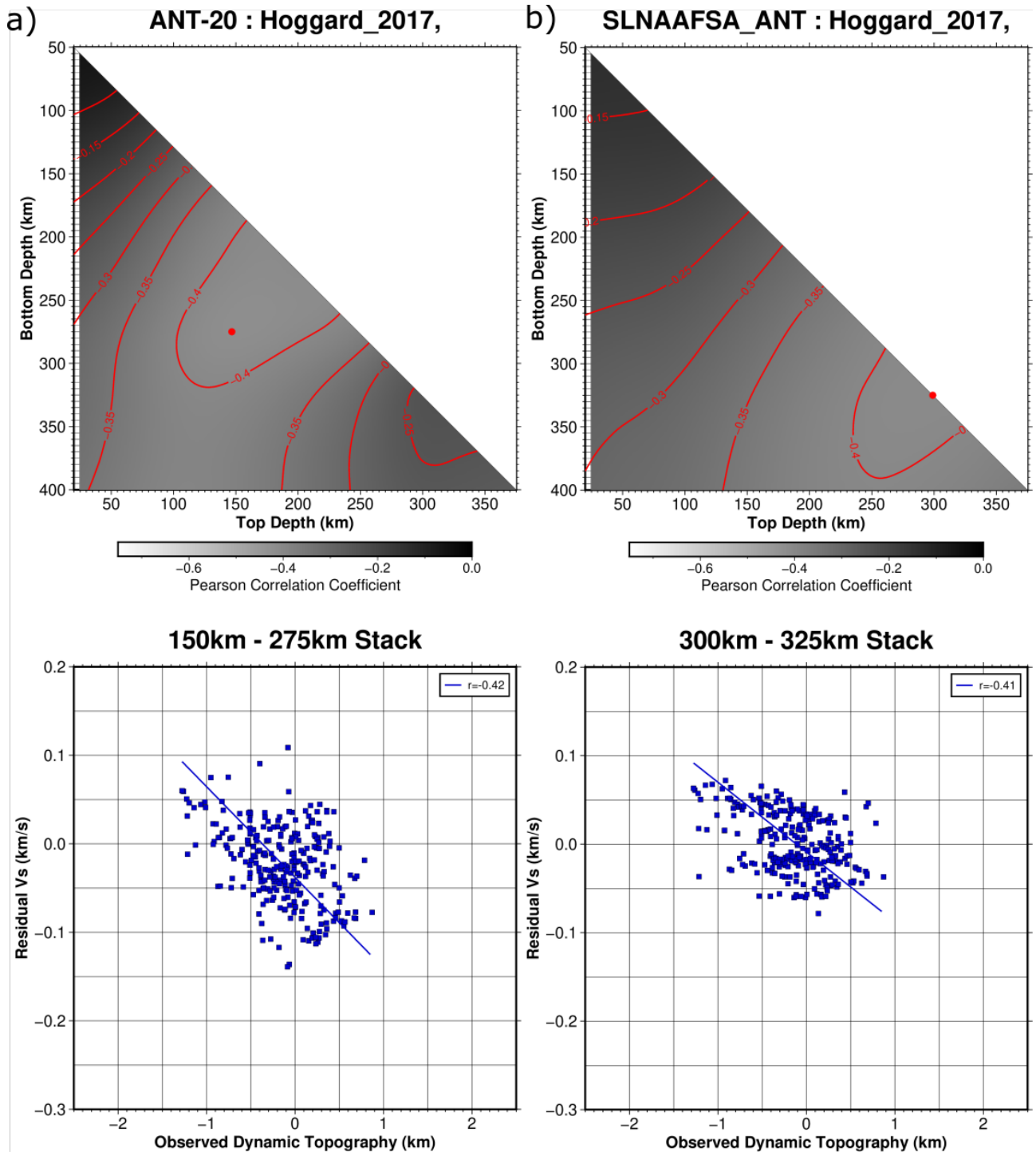


Figure 5: Heatmaps showing correlation between Hoggard et al. (2017) residual topography and residual V_S stacked over a combination of depths defined by top and bottom stacking depths. Data distribution and line of best fit plotted below for best-fitting correlation. **a)** compares ANT20 (Lloyd et al., 2020). **b)** compares SLNAAFSA Hoggard et al. (2020a) for the same region as ANT20.

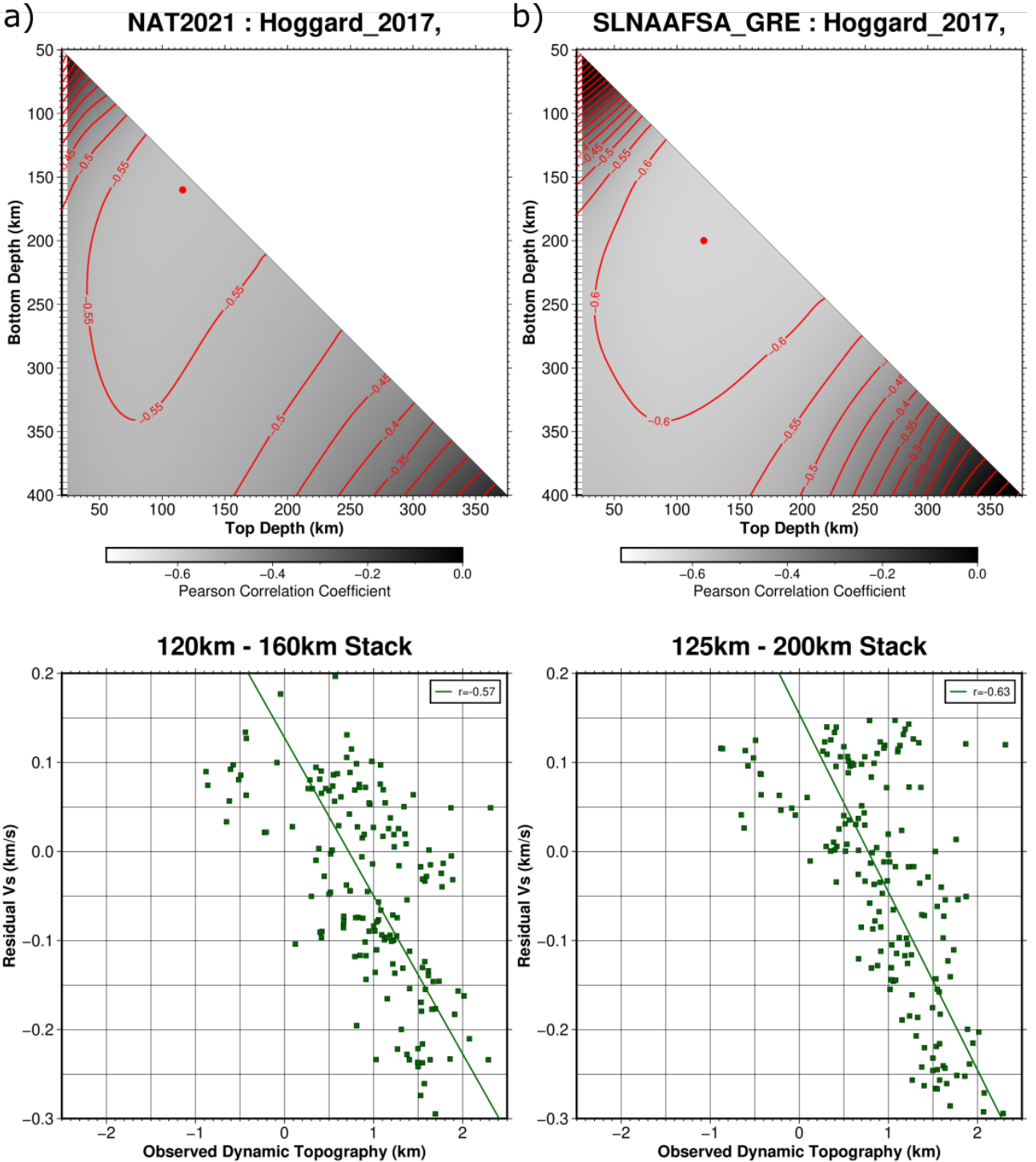


Figure 6: Heatmaps showing correlation between [Hoggard et al. \(2017\)](#) residual topography and residual V_S stacked over a combination of depths defined by top and bottom stacking depths. Data distribution and line of best fit plotted below for best-fitting correlation. **a)** compares NAT2021 ([Celli et al., 2021](#)). **b)** compares SLNAAFSA [Hoggard et al. \(2020a\)](#) for the same region as NAT2021.

depth slices. ANT-20, best correlates at 150–275 km, giving similar correlation coefficients but over a much greater sub-lithospheric depth extent. For Greenland (Figure 6) both NAT2021 and SLNAAFSA have good correlations, ~ 0.6 , over a wide range of depths. These results indicate, of the two regional models, only ANT-20 is likely to improve the accuracy of existing DT predictions. In the subsequent section ANT-20 is therefore merged with SLNAAFSA to produce new mantle convection simulations, while NAT-2021 is discarded.

2.3 Discussion

Strong correlation of isostatically optimal T_p with published petrological estimates point to Iceland-plume-derived mantle depletion as the cause of systematic offset in Greenland RT values. [Hoggard et al. \(2020b\)](#) calculated hotspot heat fluxes using volumes of associated surface swells using the [Hoggard et al. \(2017\)](#) RT data and found Iceland plume flux significantly larger than that of other hotspots. My results would imply that some of the elevated topography surrounding the Iceland plume originates from lithospheric chemical anomalies rather than sub-plate dynamic support, implying a reduction in estimated plume flux back towards that of other large hotspots.

Whilst the DT-RT discrepancy seen in Baffin Bay this may arise from poor imaging of the below mantle structure beneath, given its narrowness and SLNAAFSA's limited horizontal resolution (~ 600 km [Hoggard et al. \(2020a\)](#)), it may also be explained by melt depletion. The Iceland plume may have chemically depleted the lithosphere during its formation ~ 60 million years ago ([Antonijevic and Lees, 2018](#)), causing RT to be ~ 0.8 km higher than predictions, approximately matching the difference seen.

The main Antarctic RT-DT discrepancy may result from the lack of correction for flexural impacts of large sediment loads in the RT data. These RT measurements lie exactly on the edge of a 4 km thick sedimentary pile, seen in [Wobbe et al. \(2014\)](#). In their study, residual basement depths are calculated, ranging 0.5 - 2.0 km and matching DT predictions. [Hoggard et al. \(2017\)](#) acknowledge that this effect is not considered, as they state the relatively small flexural wavelength, should average out in their methods (see Appendix A.1.1).

3 Temperature, Convection and Dynamic Topography Models

3.1 Methodology

Calculating mantle flow evolution requires specification of an initial temperature model to infer physical properties like density and viscosity. ANT-20 and SLNAAFSA therefore need to be combined in temperature (rather than density) space. [Hazzard et al. \(2023\)](#) previously made the relevant temperature files for ANT-20, using a Bayesian inverse approach, calibrating optimised laboratory-derived parameterisations of rock anelasticity that self-consistently converts V_s into thermomechanical mantle structure ([Yamauchi and Takei, 2016](#)). SLNAAFSA temperature files were produced using an identical approach. A major benefit of this methodology is that it accurately accounts for anelastic non-linear reduction in V_s at near-solidus temperatures, preventing overestimation of shallow-mantle temperatures that occurs when linear scaling factors are instead used for the conversion. Predicted temperatures for ANT-20 further its incorporation into this model, since the hottest asthenospheric anomalies in ANT-20 correlate better with locations of Neogene-Quaternary intraplate volcanism ([Ball et al., 2021](#)) than those in SLNAAFSA (Figure 7).

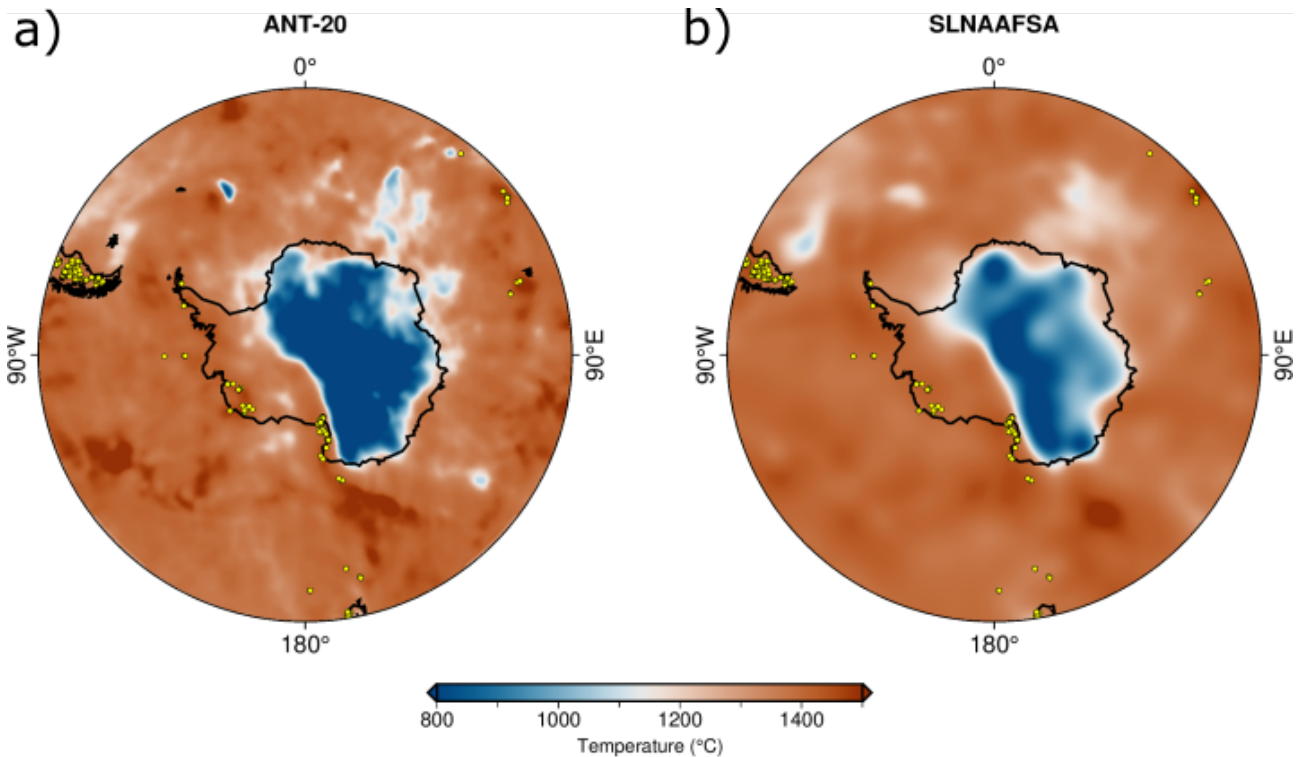


Figure 7: Maps showing different temperature models, at 150 km depth, beneath Antarctica. Yellow dots are locations of Neogene-Quaternary volcanism from [Ball et al. \(2021\)](#). **a)** ANT-20 ([Lloyd et al., 2020](#)). **b)** SLNAAFSA ([Hoggard et al., 2020a](#)) globally.

3.1.1 Model Merge

ANT-20 and SLNAAFSA temperatures were merged into a single global model, using ANT-20 up to 45°S, and SLNAAFSA elsewhere. Three methods were considered to merge the temperature predictions (Figure 8): a simple replacement (no blending), GMT’s `grdbblend` method, and a spherical harmonic (SPH) merging approach ([Adourian and Frost, 2022](#)). Whilst large-scale features continue across the boundary in the simpler methods, a division between models is still clearly visible. `Grdbblend` requires significant down-weighting of ANT-20 to smooth the boundary, which removes important details of the higher-resolution model. As a result, the SPH method was selected.

This methodology merges regional and global models by applying a mask in SPH space, tapering the regional model’s contribution to 0 at its boundaries, and summing it with the global model to create a smooth transition. An alteration to the method was made due to issues with amplitude inflation in Antarctica. The method now additionally inversely tapers the global model down to a defined boundary (51°S), meaning a transition region is created in which models are effectively averaged with their contributions scaling in opposite directions. This merged model contains only SLNAAFSA data above 45°S and only ANT-20 below 51°S. (See Appendix A.1.2 for further details.)

3.1.2 Convection and Dynamic Topography Models

The convection modelling software ASPECT ([Heister et al., 2017; Kronbichler et al., 2012](#)) was used to model whole-mantle convective flow and associated DT change back to the MPWP. Before incorporating the merged temperature model into ASPECT simulations, it needed reformatting and combining with a lower-mantle model.

The method of [Richards et al. \(2023a\)](#) was followed to generate ASPECT inputs and final

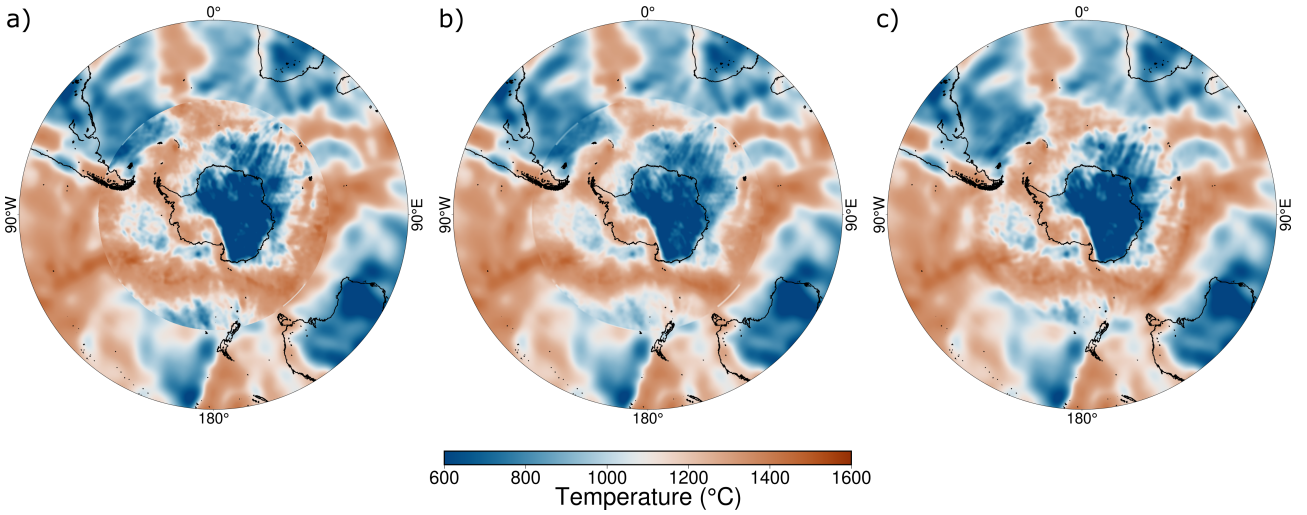


Figure 8: Maps showing temperature models at 75 km depth below Antarctica, up to -20°S, merging ANT-20 ([Lloyd et al., 2020](#)) and SLNAAFSA ([Hoggard et al., 2020a](#)). **a)** No blending. **b)** Grids merged using GMT grdblend. **c)** Grids merged using a modified version of S. Adourian’s tomography merging code ([Adourian and Frost, 2022](#)).

convection models. First, input upper-mantle temperatures are modified to ensure regions of continental lithosphere remain neutrally buoyant. The lithosphere–asthenosphere boundary was defined as the depth to the 1175°C isotherm, with temperatures at each depth within the continental lithosphere set to the mean value of all mantle material outside that region.

For temperatures in the lower mantle (below 300 km) thermodynamic model outputs are used to convert V_s tomography models into temperature. Tomography models S40RTS and LLNL-G3D-JPS are used alongside an ambient mantle viscosity profile, F10V1 ([Ritsema et al., 2011](#); [Simmons et al., 2015](#); [Forte et al., 2010](#)). Other models ([Auer et al., 2014](#); [French and Romanowicz, 2015](#); [Grand, 2002](#); [Steinberger et al., 2010](#)) were used but not carried forwards to convection modelling, as the chosen models produced DT estimates most consistent with Australian RT and Pliocene relative sea-level indicators in [Richards et al. \(2023a\)](#). The V_s models are high-pass filtered to remove vertical smearing at mid-mantle depths, then converted into temperature using thermodynamic look-up tables, computed using Perple_X, and corrected to account for anelastic effects. Large low velocity provinces (LLVPs) are defined and assigned different densities and viscosities to ambient mantle (see [Richards et al., 2023a](#)). The upper and lower mantle temperature models are then merged via linear interpolation between 300 and 400 km depth.

Backwards advection is used to calculate mantle convection and DT change back through time, reversing mantle flow directions by inverting the sign of gravity ([Moucha et al., 2008](#)). This ignores diffusive processes since they are not time-reversible, however this simplification has negligible impact over shorter timescales up to 30 Myr, hence the method is valid here (3 Ma) ([Richards et al., 2023a](#)). Simulations solve the Navier-Stokes equations using the Boussinesq approximation, which simplifies computations by assuming constant density in inertial terms, but not the buoyancy term ([Heister et al., 2017](#); [Kronbichler et al., 2012](#)). Still following [Richards et al. \(2023a\)](#), DT was calculated at each timestep via surface normal stresses. These fields were then rotated according to assumed plate motions, and the resulting field subtracted from present day fields to obtain DT change. Plate motions were defined using two different models: ‘MORVEL’ ([DeMets et al., 2010](#)), based on modern GPS data with the assumption plate motions have not changed since the Pliocene (~ 3 Ma); and ‘GPlates’ ([Seton et al., 2012](#)), which uses mantle hotspot tracks and oceanic magnetic anomalies to reconstruct plate motions back through time. Present-day DT was calculated using the merged model and the

methodology of [Richards et al. \(2023b\)](#).

3.2 Results

The sharpest temperature variations in the whole-mantle temperature models (Figure 9) occur at the shallowest and deepest depths, with mid-mantle temperatures more consistent. At 200 km this is expected with cooler mantle temperatures below thick lithosphere and at subduction zones. At the base of the mantle, the substantial temperature variation is mostly associated with the presence of LLVPs ([Richards et al., 2023b](#)).

The primary feature of Antarctic mantle flow predictions (Figure 10) is a hot upwelling below the Ross Sea, bordering the Transantarctic Mountains (TAM). Flow is fast here, with a radial velocity of ~ 50 mm/yr. Transect A shows a small, distinct clockwise convection loop rising to the west of the mountains and sinking to the east, below the East Antarctic craton. To the west flow is slower, directed towards the convection cell, and upper mantle temperatures are warm. At the intersection of A and C, above the main upwelling, transect C shows mostly radial motion, with a small component of motion up the transect.

Transect B, across the centre of West and East Antarctica, shows a distinct downwelling below central Antarctica, creating two larger-scale contrasting convection cells. Large, cold temperature anomalies are seen at the CMB.

Greenland mantle flow predictions are dominated by the Iceland Plume, with material near the surface moving upward and outward in a radial pattern at high velocities > 100 mm/yr. Motion elsewhere is relatively slow $< \sim 5$ mm/yr. The plume is seen clearly in transect, with strong vertical motion, and a hot anomaly at the CMB. Cold temperatures are seen in the upper mantle in Northern and Southern Greenland, whilst a warm anomaly is seen below Eastern Greenland in the lower mantle.

Antarctic DT change since 3 Ma (Figure 12) is most prominent in the Ross Sea, along the edge of the TAM aligning with the convective upwelling. Here, ~ 400 m uplift has occurred since 3 Ma in all models. However, this study finds a much thinner, linear band of uplift along the edge of the craton, unlike [Austermann et al. \(2015\)](#) models (hereafter A15), which find a wider, circular pattern. Inclusion of a higher resolution seismic model (ANT-20) has refined features with respect to previous models. More uplift across West Antarctica is seen compared to previous models, particularly in Marie Byrd Land, meaning it likely sat lower than previously thought during the MPWP, reducing WAIS stability at this time. The EA coast sees substantial uplift, particularly in Dronning Maud Land. Unlike [Austermann et al. \(2015\)](#), this study finds mostly subsidence in Wilkes Basin rather than uplift, indicating that the ice sheet in this region may have been more stable during the MPWP than at present.

Differences in Greenland between this study and [Richards et al. \(2023a\)](#) are expected to be minimal, as both use temperature structure from SLNAAFSA in the upper mantle. DT distributions are identical, with slight differences in amplitude, which occur due to minor differences in LLVP thickness and density offset parameters, with this study adopting a slightly thicker basal LLVP layer and lower density contrast. Models show significant uplift since the Pliocene around the Iceland hotspot, up to 400 m, and low-amplitude subsidence in Greenland, with greater amplitudes below Baffin Bay. This means higher bedrock is expected to have existed across Greenland in the Pliocene.

Inclusion of ANT-20 in present-day DT models has minor improvements in correlation with RT relative to an SLNAAFSA-only model (see Appendix A.1.3 for more detail).

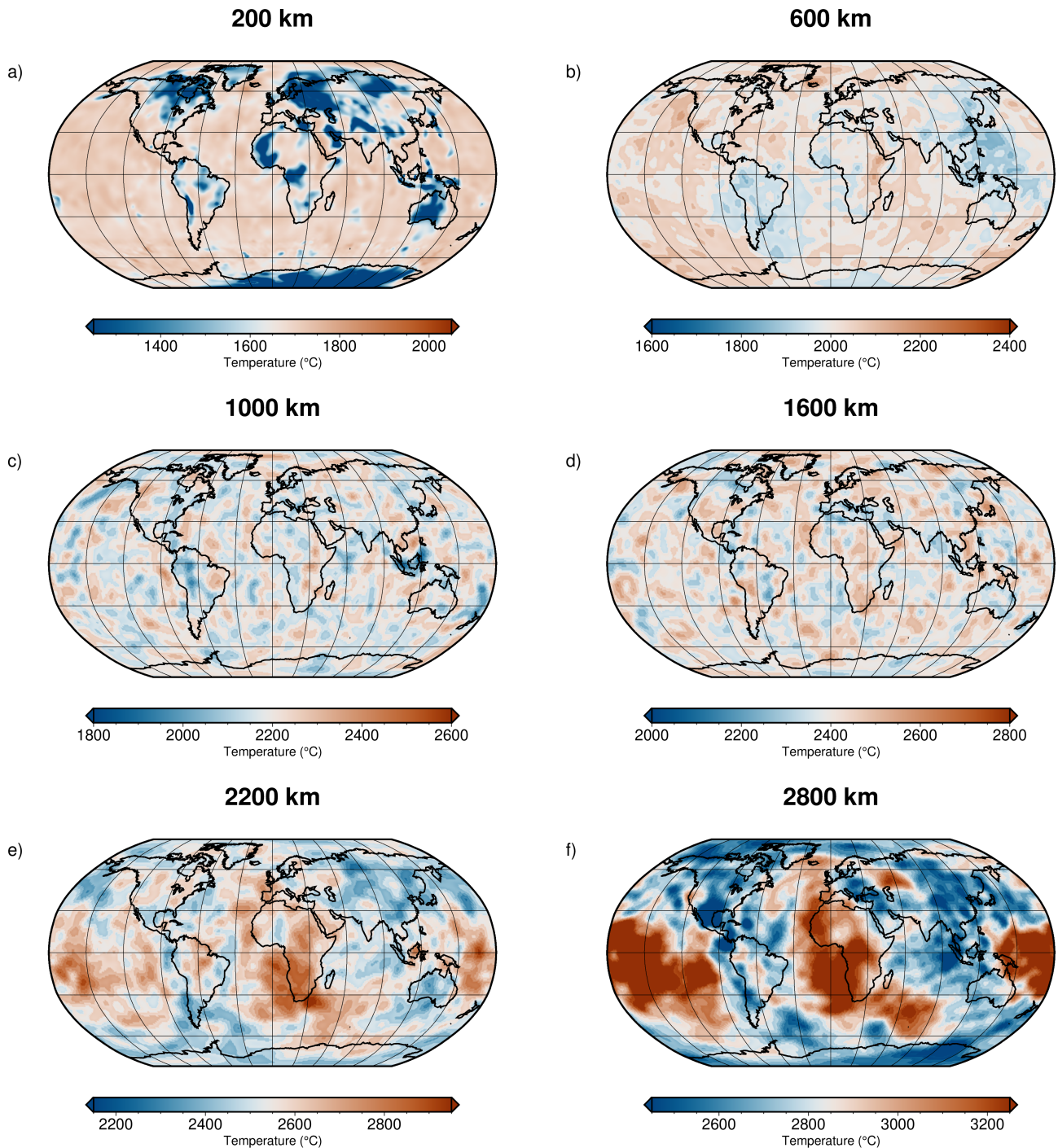


Figure 9: Maps showing ASPECT input temperatures derived using S40RTS lower mantle tomography (Ritsema et al., 2011). Temperature scales range $\pm 400^\circ\text{C}$ from the slice average temperature. a) - f) show depths 200, 600, 1000, 1600, 2200, 2800 km respectively.

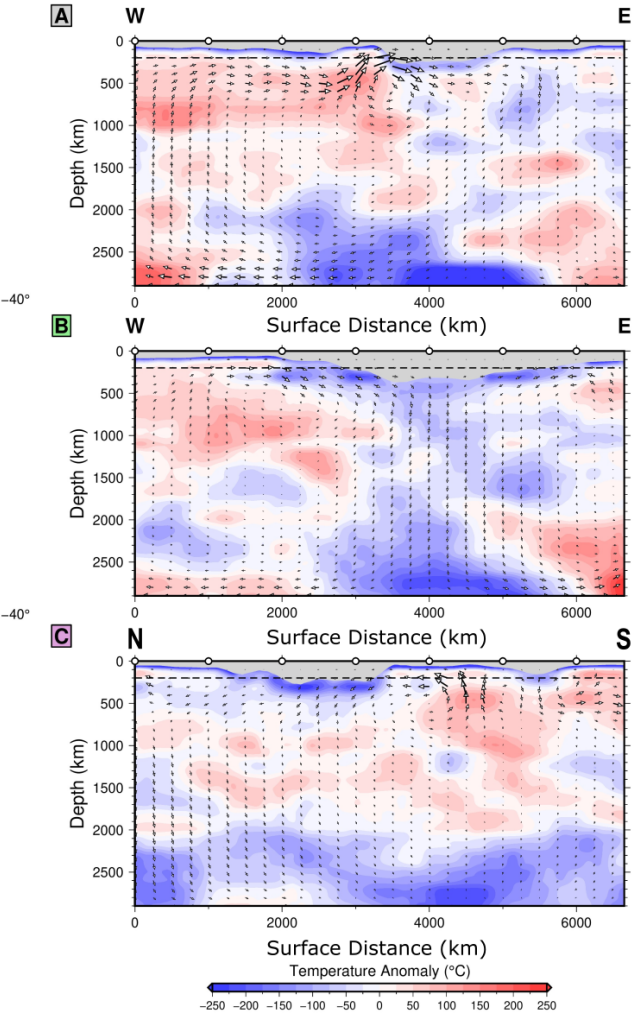
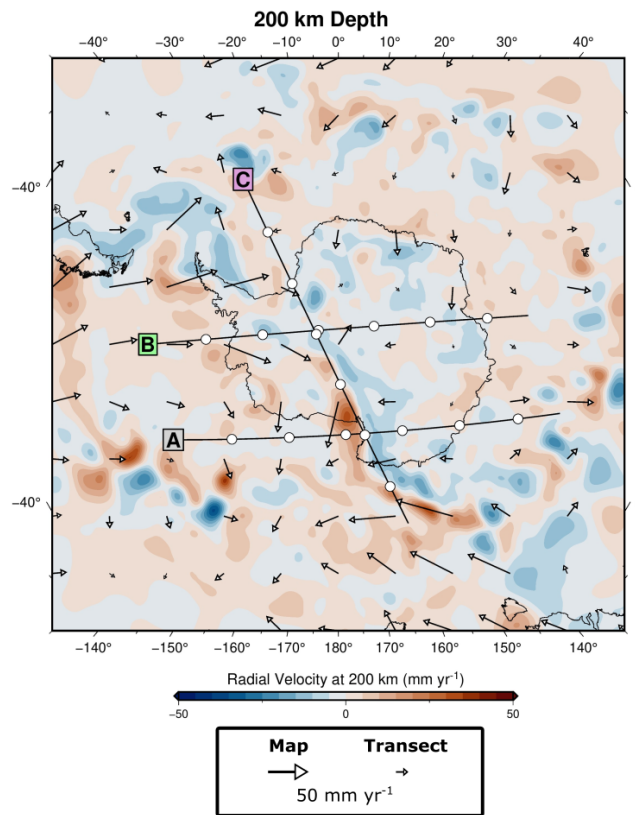


Figure 10: Map of mantle convection model, using S40RTS lower-mantle model ([Ritsema et al., 2011](#)), at 200km depth below Antarctica. Arrows represent latitudinal and longitudinal components of motion, and colour represents radial motion. **A**, **B** and **C** are radial cross-sections as labelled on the map, extending to the CMB. Arrows represent vertical and along-azimuth components of motion, and colours represent temperature anomaly from a 1330°C adiabat. White circles along transects are spaced every 1000 km. At depth, cross-sections are horizontally exaggerated.

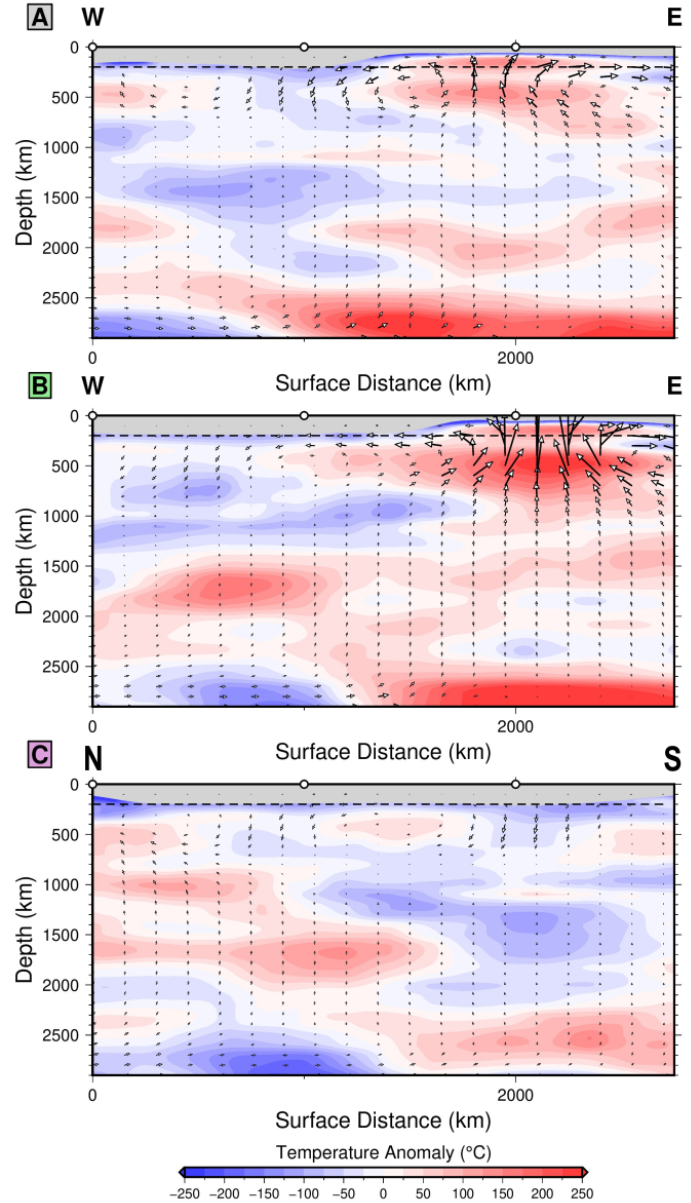
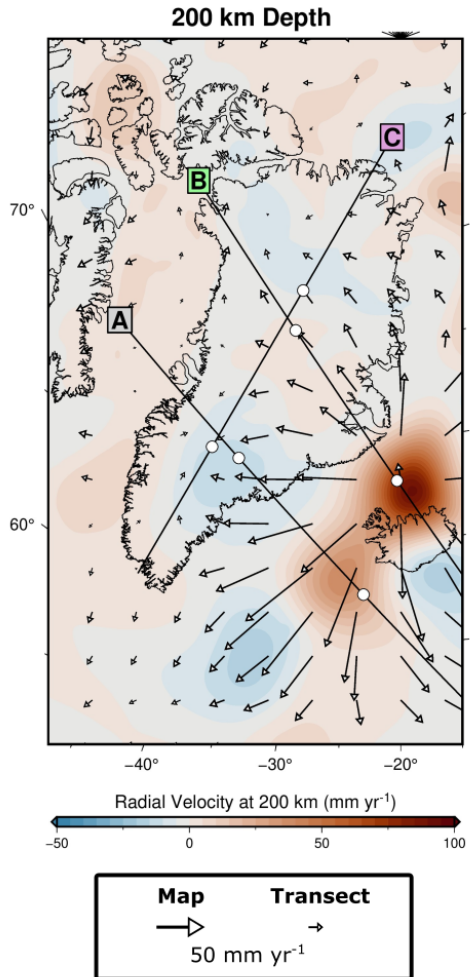


Figure 11: Map of mantle convection model, using S40RTS lower-mantle model (Ritsema et al., 2011), at 200 km depth below Greenland. Arrows represent latitudinal and longitudinal components of motion, and colour represents radial motion. **A**, **B** and **C** are radial cross-sections as labelled on the map, extending to the CMB. Arrows represent vertical and along-azimuth components of motion, and colours represent temperature anomaly from a 1330°C adiabat. White circles along transects are spaced every 1000 km. At depth, cross-sections are horizontally exaggerated.

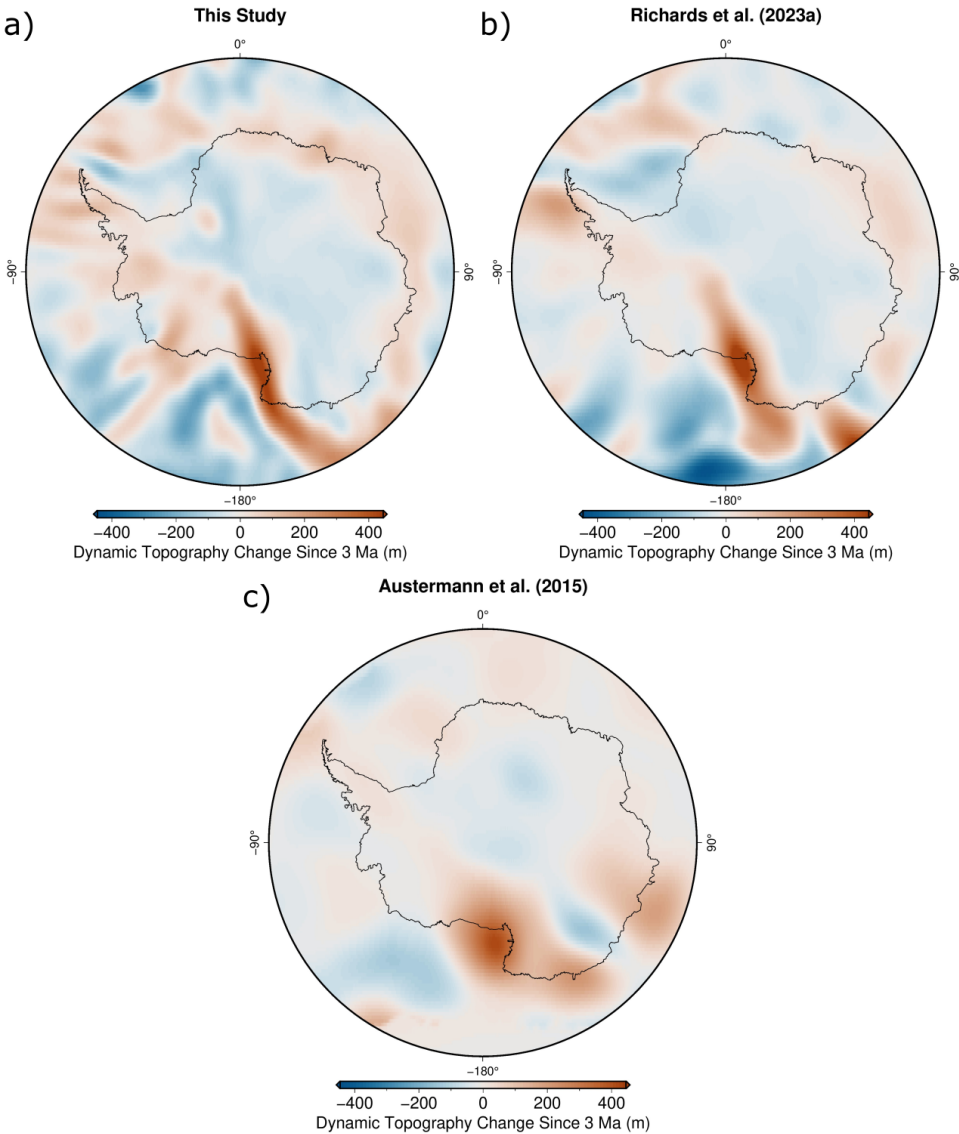


Figure 12: Maps of Antarctica showing the change in dynamic topography since 3 Ma in three different studies using plate motions from *DeMets et al. (2010)*. **a)** This study. **b)** *Richards et al. (2023a)*. **c)** *Austermann et al. (2015)*.

3.3 Discussion

Key features seen in the new mantle convection models are in agreement with those expected in the literature. The Ross Sea convection cell is seen in *Austermann et al. (2015)*, who attribute motion to corner flow around the edge of the craton. Their models show two distinct counter-rotating cells, with material rising from the lower mantle below EA and diverging at the main anomaly. This study sees material flowing laterally from warm upper mantle temperatures, with a weak upwelling below the Amundsen Sea, creating corner flow where obstructed by the craton. *Lloyd et al. (2020)* discusses low shear-wave speed anomalies here in ANT-20, and attributes them to remnants of Cenozoic extension with lingering warm mantle temperatures, with similar explanations given for convection patterns in A15. Large cold anomalies below Antarctica at the CMB coincide with proposed slab graveyards, the result of significant historical subduction in West Antarctica, including of the Phoenix Plate (*Lloyd et al., 2020; Sutherland et al., 2010*).

In Greenland, cold, upper-mantle anomalies coincide with known cratons as seen in NAT2021 (*Celli et al., 2021*). Warm temperatures below Eastern Greenland are seen in the lower mantle. NAT2021 images the Iceland Plume bending beneath Eastern Greenland in the transition zone,

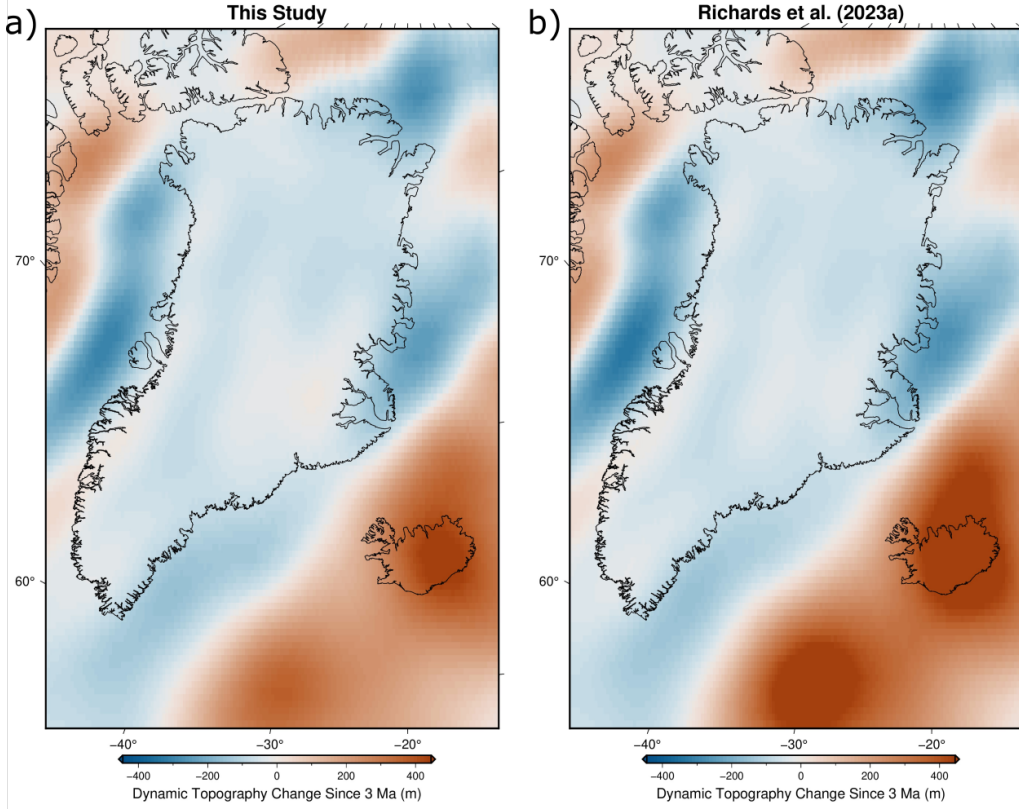


Figure 13: Maps of Greenland showing the change in dynamic topography since 3 Ma in two different studies using plate motions from [DeMets et al. \(2010\)](#). **a)** This study. **b)** [Richards et al. \(2023a\)](#).

though is only an upper-mantle model. This study finds mantle flow velocities around Iceland that also match those expected in the literature. V-shaped ridges seen around Iceland, which form as plume material propagates radially outwards while the overlying plates spread apart, require differing plume material and plate-spreading velocities to form their distinctive shape ([Hoggard et al., 2020b](#)). [Poore et al. \(2009\)](#) found that these features require plume material to move laterally at 87–282 mm/yr, in agreement with these convection models (~ 100 mm/yr).

4 Palaetopography and Ice-sheet Models

4.1 Methodology

To isolate the impact of post-Pliocene bedrock topography change on ice-sheet stability, calculated DT changes were subtracted from present-day topography ([Le Brocq et al., 2010; Bind-schadler et al., 2013](#)) to estimate MPWP palaeotopography. Ice-sheet models were run using the software PISM ([Bueler and Brown, 2009; Winkelmann et al., 2011](#)), which solves the Stokes equation for ice-sheet flow, and incorporates processes such as MISI and calving (not MICI). [Winkelmann et al. \(2011\)](#) describes the hybrid model of ice-sheet flow used, which combines the Shallow Ice Approximation (SIA) and the Shallow Shelf Approximation (SSA). SIA is used to model the ice-sheet interior, where its base is frozen to bedrock, and ignores longitudinal stresses, as vertical shear dominates. SSA is useful for modelling fast-flowing ice, like ice shelves or streams, where basal resistance is close to zero and longitudinal stresses dominate. PISM uses a hybrid formulation, with SSA used to model sliding in regions where basal resistance is lowered due to basal melt or till ([Bueler and Brown, 2009](#)). SIA and SSA velocities are calculated for the whole ice-sheet and summed, with those obtained from the most appropriate

approximation naturally dominating the total [Winkelmann et al. \(2011\)](#).

Antarctic ice-sheet models were run following the methods of [Martin et al. \(2011\)](#), using a pseudo-plastic till parameter, which allows plastic till behaviour up to a certain yield strength. For Greenland, models followed PISM examples as described in [Bindschadler et al. \(2013\)](#). Both ice-sheets' models use data from the SeaRISE project for modern basal heating, ice thickness and bedrock topography ([Bindschadler et al., 2013](#)).

Models were run using both modern topography and predicted MPWP palaeotopographies. The MPWP reference model adopts palaeotopography predicted using the MORVEL plate-motion model ([DeMets et al., 2010](#)) and S40RTS lower-mantle tomography ([Ritsema et al., 2011](#)), and allows bedrock topography to evolve with changing ice loads according to a viscoelastic Earth model with an 88 km thick elastically deforming lithosphere (flexural rigidity = 5×10^{24} N m) underlain by viscously deforming mantle (viscosity = 10^{21} Pa s ([Bueler et al., 2007](#); other models, including fixed-bed runs, in Appendix A.2.2)). Here, I aim to isolate the contribution of DT-induced bedrock topography change to MPWP-to-present shifts in equilibrium ice volume from that caused by climate change. Fortunately, [Paxman et al. \(2020\)](#) showed that, despite differences in *absolute* ice volume, bedrock topography change causes approximately the same *relative* shift in ice volume when forced with cold (~ modern) and warm (\$sim MPWP) climatic inputs. We therefore adopt modern climatic inputs in the ice-sheet model runs, since our estimates of DT-induced ice volume change are expected to be independent of climate forcing. Adopting modern values is both simpler and enables model outputs to be checked against modern satellite constraints. Note that [Austermann et al. \(2015\)](#) did adopt Pliocene climatic forcing in their ice-sheet simulations with DT-corrected bedrock topography. To enable direct comparison, A15 palaeotopography is incorporated into new simulations that adopt identical climatic, ice-sheet and bed-response conditions to the reference model.

Following [Martin et al. \(2011\)](#), models were 'spun-up' multiple times, with each spin-up increasing in parameterisation complexity. This incremental approach ensures the model is initialised in a stable configuration and is able to reach a sensible steady-state in the full complexity final runs. In the final spin-up, models were allowed 100 kyr to reach equilibrium. For each MPWP palaeotopography model run, maps of ice thickness and change relative to models initialised with modern topography were produced, alongside ice-volume timeseries plots (Appendix A.2.2).

4.2 Results

In Antarctica, the clearest palaeotopographic change is in the Ross Sea, along the TAM, where bedrock sits \sim 1500 m below sea level. The Recovery Basin is divided by bedrock above sea level in Pliocene models, which may improve ice-sheet stability and restrict grounding line retreat. Other changes, particularly in WA, are harder to visualise, due to changes being on the order of \sim 50 m in areas over 1000 m below sea level. Whilst vertical changes are small ($< \pm 200$ m) they may significantly influence ice-sheet stability since low topographic gradients across Antarctica spread the impact of vertical motions across wide geographic areas. WA is mostly deeper in Pliocene models, particularly Marie Byrd Land and the Ross Sea, suggesting ice in these regions was more susceptible to retreat during the MPWP than expected. Unlike [Austermann et al. \(2015\)](#), Wilkes Basin is somewhat shallower in the Pliocene, though still marine-based.

Greenland Pliocene palaeotopography is generally higher, with areas in the West and North rising above sea level. Many coastal glacial outlets, particularly in the South East, rise above sea level, suggesting the GIS may have been naturally more stable during the MPWP.

The clearest bedrock-induced AIS change (Figures 16, 15) is in the Ross Sea, where the entire ice shelf is lost and retreats into Marie Byrd Land. Ice thicknesses here reduce over 3000 m. Whilst the A15 palaeotopography simulation also predicts thinning here, there is not

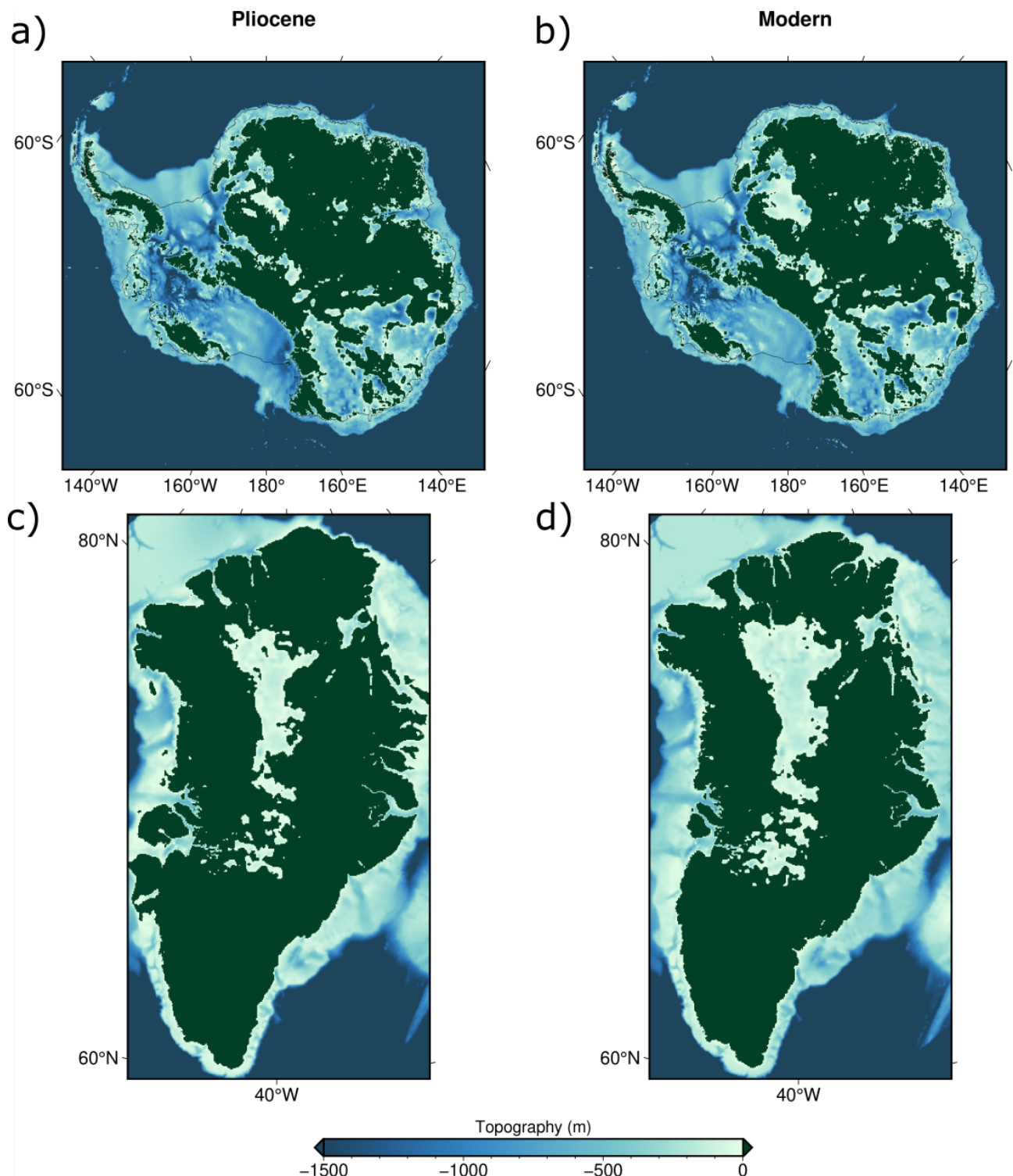


Figure 14: a), c) Maps of predicted MPWP topography for Antarctica and Greenland, respectively. b), d) Maps of modern topography for Antarctica and Greenland respectively. MPWP topography assumes MORVEL plate model (*DeMets et al.*, 2010) and S40RTS lower-mantle model. Modern topographies from *Le Brocq et al.* (2010) and SeaRISE (*Bindschadler et al.*, 2013). All topography above sea level coloured green to highlight marine-based changes.

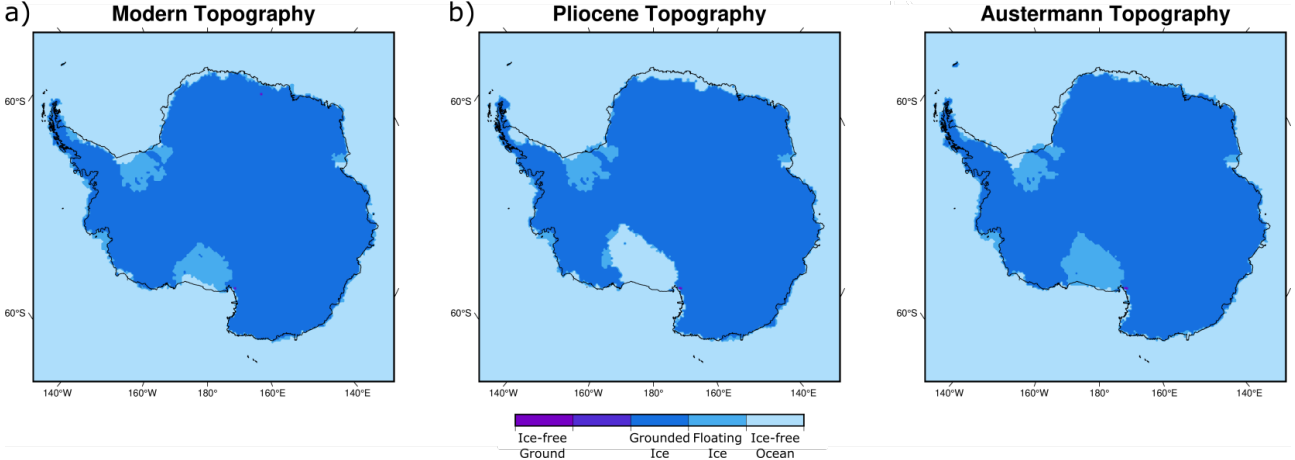


Figure 15: Maps of Antarctic ice type for MPWP reference model (MORVEL plate model ([DeMets et al., 2010](#)) and S40RTS lower-mantle model ([Ritsema et al., 2011](#)) on a viscoelastically deforming bed). Background topography is ETOPO bedrock data from [NOAA National Centers for Environmental Information \(2022\)](#). **a)** Modern topography ice-sheet model. **b)** Pliocene-corrected topography ice-sheet model. **c)** Ice-sheet model from [Austermann et al. \(2015\)](#).

complete ice loss. Other notable areas of change are the Antarctica Peninsula and coast of Dronning Maud Land, which show significantly more retreat in the MPWP reference model than in the A15 run. The 400 km retreat of Wilkes Basin is not seen in the A15 model due to the use of modern climate conditions, however substantial thinning is observed, which is not present in the reference model. Antarctica, on average, experienced minor thinning on the order of ~ 100 metres. The MPWP reference model holds 1.8 m less of sea-level equivalent (SLE) than its modern counterpart. Minimal differences in this relative offset are seen in other models (Appendix A.2.2), with fixed-bed runs representing the most extreme scenarios.

Greenland experiences little bedrock-induced ice volume change overall (Figure 17), though significant thickening (~ 1000 m) is seen in the MPWP reference model at Helheim Glacier, which extends further seaward compared to today. The ice-sheet also thickens along the north-western coastline. Eastern Greenland, in general, sees minor thickening whilst western and northern areas thin. Overall, total ice volume increases by 0.12 m SLE when DT-corrected MPWP palaeotopography is adopted instead of modern values.

4.3 Discussion

These results highlight both the relevance of DT change to modelling Pliocene ice sheets and sea levels, and the importance of accurate, high-resolution seismic tomography datasets to better quantify the spatiotemporal changes in ice-sheet stability it has induced. The MPWP-to-modern increase in stability of the Ross Ice Shelf found in this study and of the Wilkes Basin ice-sheet found in [Austermann et al. \(2015\)](#), occurs in response to uplift caused by the same upwelling structure. However, due to the differing resolutions of the tomographic models used to predict this mantle flow, the resulting DT and ice-sheet changes are distributed differently, with model features in this study more clearly resolved in shape and location. Whilst amplitudes of DT change are similar to those in the A15 models, the differing spatial distribution of uplift and subsidence leads to the loss of an extra 0.3 m SLE compared to the modern reference model.

In Antarctica, DT alone can account 1.8 m of the Antarctic contribution to higher MPWP GMSL, with the remainder presumably reflecting warmer climatic conditions during this time. [DeConto et al. \(2021\)](#) calibrated ice-sheet model instability parameters by assuming a target Antarctic MPWP GMSL contribution of $\sim 16 \pm 5$ m, with the majority of their optimised pa-

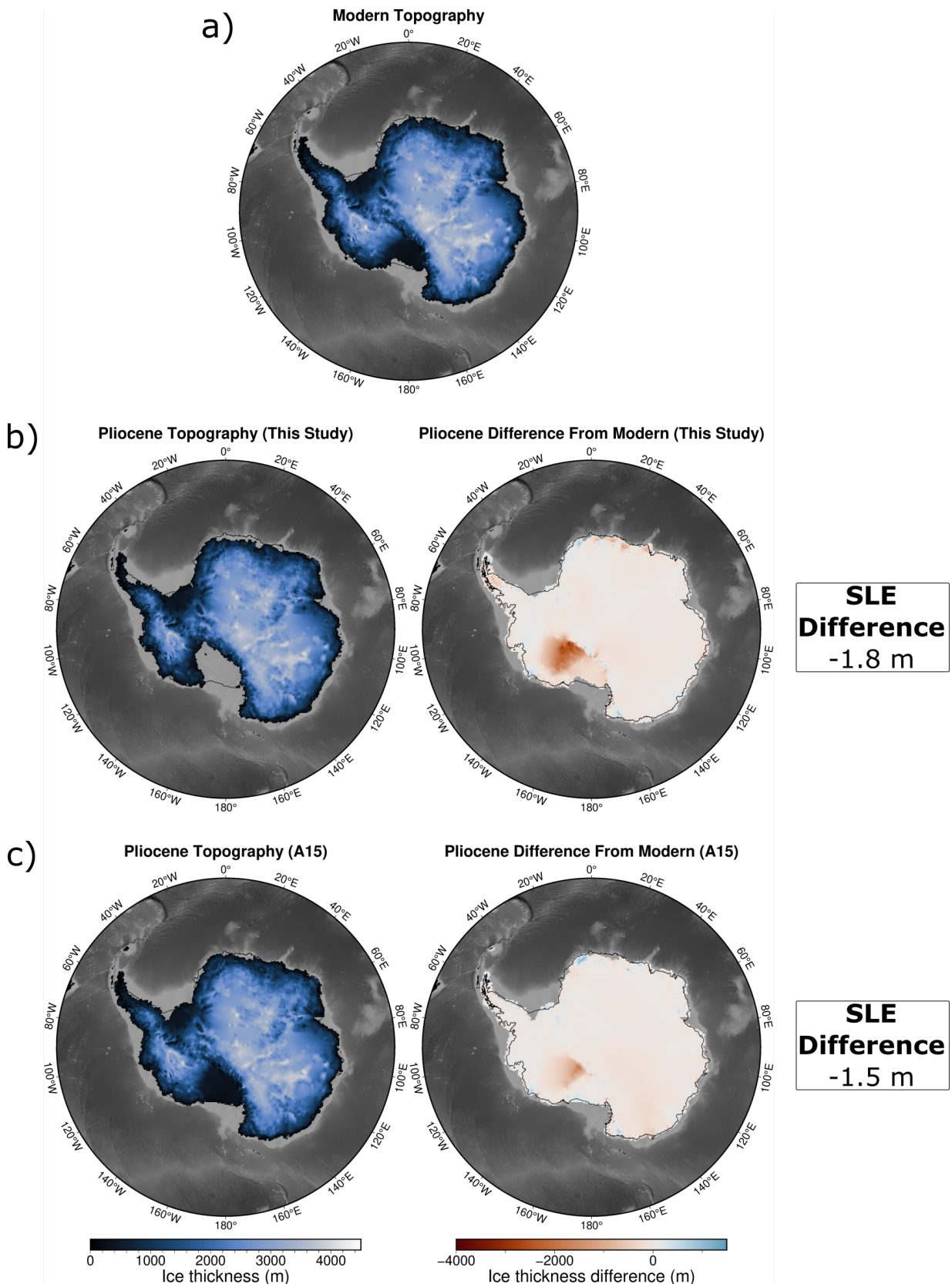


Figure 16: Maps of Antarctic ice thickness for MPWP reference model (MORVEL plate model (*DeMets et al.*, 2010) and S40RTS lower-mantle model (*Ritsema et al.*, 2011) on a viscoelastically deforming bed). Background topography is ETOPO bedrock data from *NOAA National Centers for Environmental Information* (2022). SLE difference represents change in sea-level equivalent stored in ice-sheet relative to modern reference model. **a)** Modern topography ice-sheet model. **b)** Left: Pliocene-corrected topography ice-sheet model. Right: Difference of Pliocene ice-thickness from modern. **c)** Ice-sheet model from *Austermann et al.* (2015) (A15). Left: Pliocene Ice thickness. Right: Pliocene ice-thickness difference from modern.

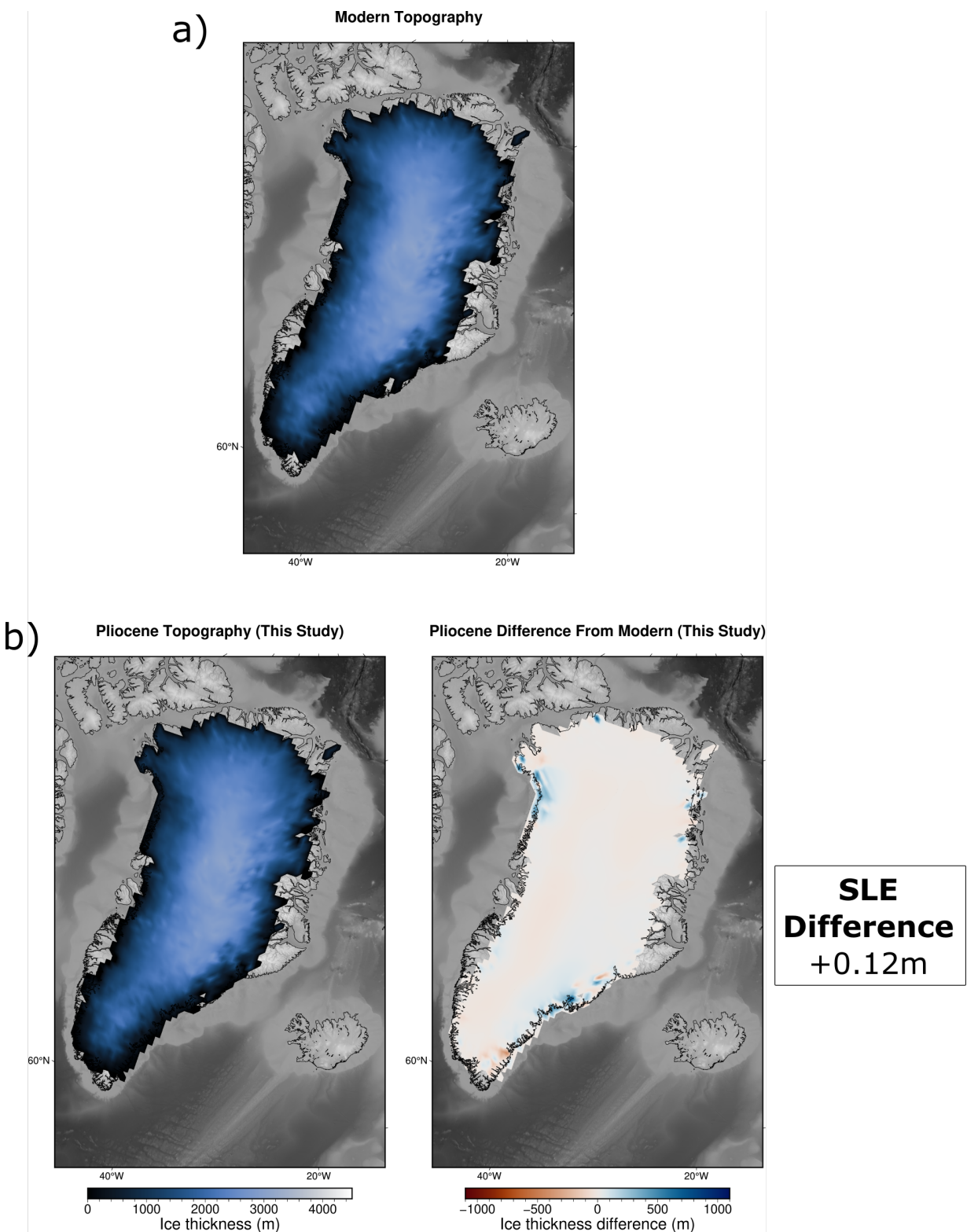


Figure 17: Maps of Greenland ice thickness for MPWP reference model (MORVEL plate model (*DeMets et al.*, 2010) and S40RTS lower-mantle model (*Ritsema et al.*, 2011) on a viscoelastically deforming bed). Background topography is ETOPO bedrock data from [NOAA National Centers for Environmental Information \(2022\)](#). SLE difference represents change in sea-level equivalent stored in ice-sheet relative to modern reference model. **a)** Modern topography ice-sheet model. **b)** Left: Pliocene-corrected topography ice-sheet model. Right: Difference of Pliocene ice-thickness from modern.

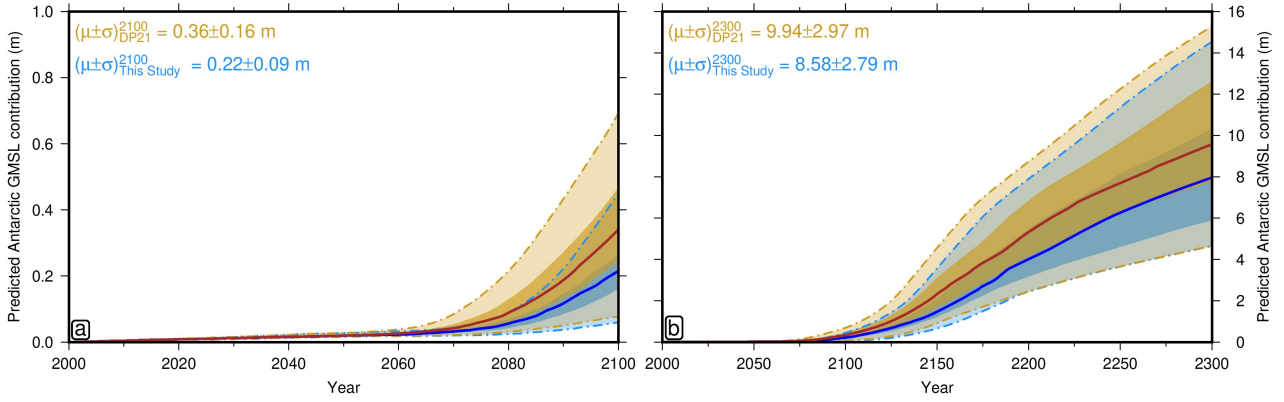


Figure 18: Plots following [Richards et al. \(2023a\)](#) showing GMSL rise based on models of [DeConto et al. \(2021\)](#) for a high emissions scenario due to AIS melting **a)** over this century (2000 - 2100) **b)** up to 2300. Yellow line / shading represent original results from [DeConto et al. \(2021\)](#). Blue lines / shading represent results from this study, where 1.8 m SLE difference caused by post-Pliocene DT change (calculated using the MORVEL plate model ([DeMets et al., 2010](#)) and S40RTS lower-mantle model) is removed from original [DeConto et al. \(2021\)](#) estimate of AIS contribution to MPWP GMSL (16 ± 5 m). Solid lines are median model values, dark shading represents 50% confidence, light shading represents 99% confidence.

parameterisations predicting ice losses close to this upper GMSL bound. While their MPWP models account for differences in climatic forcing, they assume modern bedrock topography. My findings therefore suggest their target GMSL bounds should be lowered by 1.8 m, which suggests several of their calibrated parameterisations are no longer consistent with Antarctic MPWP GMSL estimates, including their preferred model. Following [Richards et al. \(2023a\)](#), the [DeConto et al. \(2021\)](#) sea-level projections were recalibrated using this lowered target (Figure 18). Although this is only a 1.8 m SLE reduction in the assumed climatic contribution to Antarctic ice loss during the MPWP, this change is sufficient to exclude many of their more unstable model parameterisations. As a result, end-of-century AIS GMSL contributions reduce significantly from 0.36 m to 0.22 m, a ~45% drop, with similar drops in uncertainty. Although, AIS GMSL contributions by 2300 drop by only ~14% and ~6%, respectively. These findings highlight that DT-induced changes in Pliocene bedrock topography have important consequences for our understanding of ice-sheet sensitivity to climatic forcing and the likely trajectory of future sea-level change.

5 Conclusions

This study shows that DT-induced bedrock topography change has had a significant impact on MPWP-to-modern Antarctic ice-sheet evolution and highlights that accurate predictions of this change require the incorporation of high-resolution seismic constraints into mantle flow simulations. Comparison of present-day DT and RT suggests generally good agreement between predictions and observations, although a 0.8 km offset between Greenland RT measurements and co-located DT predictions was observed. This can be explained by accounting for elevated RT caused by Iceland-plume-related melt depletion of the North Atlantic mantle lithosphere. Since residual V_S and temperatures calculated for a high-resolution Antarctic tomographic model (ANT-20) correlated better than global model (SLNAAFSA) counterparts, a merged temperature model was created from these two to simulate mantle flow and predict DT change since the MPWP. Resulting predictions of post-Pliocene DT change were used to reconstruct MPWP bedrock topography and run revised ice-sheet models for Antarctica and Greenland.

Antarctic runs found that DT change accounts for 1.8 m of MPWP GMSL excess, reducing inferred ice-sheet sensitivity to climate forcing. Recalibrating recent sea-level projections using this revised constraint, lowers the expected end-of-century Antarctic contribution to future GMSL rise by ~45%.

References

- Adourian, S., and D. A. Frost (2022), A merging package for multi-scale, multi-resolution tomographic models., in *AGU Fall Meeting Abstracts*, vol. 2022, pp. S12A–10.
- Antonijevic, S. K., and J. M. Lees (2018), Effects of the Iceland plume on Greenland's lithosphere: New insights from ambient noise tomography, *Polar Science*, 17, 75–82, doi:[10.1016/j.polar.2018.06.004](https://doi.org/10.1016/j.polar.2018.06.004).
- Auer, L., L. Boschi, T. W. Becker, T. Nissen-Meyer, and D. Giardini (2014), Savani : A variable resolution whole-mantle model of anisotropic shear velocity variations based on multiple data sets, *Journal of Geophysical Research: Solid Earth*, 119(4), 3006–3034, doi:[10.1002/2013JB010773](https://doi.org/10.1002/2013JB010773).
- Austermann, J., D. Pollard, J. X. Mitrovica, R. Moucha, A. M. Forte, R. M. DeConto, D. B. Rowley, and M. E. Raymo (2015), The impact of dynamic topography change on Antarctic ice sheet stability during the mid-Pliocene warm period, *Geology*, 43(10), 927–930, doi:[10.1130/G36988.1](https://doi.org/10.1130/G36988.1).
- Ball, P. W., N. J. White, J. Maclennan, and S. N. Stephenson (2021), Global influence of mantle temperature and plate thickness on intraplate volcanism, *Nature Communications*, 12(1), 2045, doi:[10.1038/s41467-021-22323-9](https://doi.org/10.1038/s41467-021-22323-9).
- Bindschadler, R. A., S. Nowicki, A. Abe-Ouchi, A. Aschwanden, H. Choi, J. Fastook, G. Granzow, R. Greve, G. Gutowski, U. Herzfeld, C. Jackson, J. Johnson, C. Khroulev, A. Levermann, W. H. Lipscomb, M. A. Martin, M. Morlighem, B. R. Parizek, D. Pollard, S. F. Price, D. Ren, F. Saito, T. Sato, H. Seddik, H. Seroussi, K. Takahashi, R. Walker, and W. L. Wang (2013), Ice-sheet model sensitivities to environmental forcing and their use in projecting future sea level (the SeaRISE project), *Journal of Glaciology*, 59(214), 195–224, doi:[10.3189/2013JoG12J125](https://doi.org/10.3189/2013JoG12J125).
- Bueler, E., and J. Brown (2009), Shallow shelf approximation as a “sliding law” in a thermomechanically coupled ice sheet model, *Journal of Geophysical Research: Earth Surface*, 114(F3), doi:[10.1029/2008JF001179](https://doi.org/10.1029/2008JF001179).
- Bueler, E., C. S. Lingle, and J. Brown (2007), Fast computation of a viscoelastic deformable Earth model for ice-sheet simulations, *Annals of Glaciology*, 46, 97–105, doi:[10.3189/172756407782871567](https://doi.org/10.3189/172756407782871567).
- Celli, N. L., S. Lebedev, A. J. Schaeffer, and C. Gaina (2021), The tilted Iceland Plume and its effect on the North Atlantic evolution and magmatism, *Earth and Planetary Science Letters*, 569, 117,048, doi:[10.1016/j.epsl.2021.117048](https://doi.org/10.1016/j.epsl.2021.117048).
- DeConto, R. M., D. Pollard, R. B. Alley, I. Velicogna, E. Gasson, N. Gomez, S. Sadai, A. Condrong, D. M. Gilford, E. L. Ashe, R. E. Kopp, D. Li, and A. Dutton (2021), The Paris Climate Agreement and future sea-level rise from Antarctica, *Nature*, 593(7857), 83–89, doi:[10.1038/s41586-021-03427-0](https://doi.org/10.1038/s41586-021-03427-0).

DeMets, C., R. G. Gordon, and D. F. Argus (2010), Geologically current plate motions, *Geophysical Journal International*, 181(1), 1–80, doi:[10.1111/j.1365-246X.2009.04491.x](https://doi.org/10.1111/j.1365-246X.2009.04491.x).

Forte, A. M., S. Quéré, R. Moucha, N. A. Simmons, S. P. Grand, J. X. Mitrovica, and D. B. Rowley (2010), Joint seismic–geodynamic–mineral physical modelling of African geodynamics: A reconciliation of deep-mantle convection with surface geophysical constraints, *Earth and Planetary Science Letters*, 295(3-4), 329–341, doi:[10.1016/j.epsl.2010.03.017](https://doi.org/10.1016/j.epsl.2010.03.017).

French, S. W., and B. Romanowicz (2015), Broad plumes rooted at the base of the Earth's mantle beneath major hotspots, *Nature*, 525(7567), 95–99, doi:[10.1038/nature14876](https://doi.org/10.1038/nature14876).

Grand, S. P. (2002), Mantle shear-wave tomography and the fate of subducted slabs, *Philosophical Transactions of the Royal Society of London. Series A: Mathematical, Physical and Engineering Sciences*, 360(1800), 2475–2491, doi:[10.1098/rsta.2002.1077](https://doi.org/10.1098/rsta.2002.1077).

Hazzard, J. A., F. D. Richards, S. D. Goes, and G. G. Roberts (2023), Probabilistic Assessment of Antarctic Thermomechanical Structure: Impacts on Ice Sheet Stability, *Journal of Geophysical Research: Solid Earth*, 128(5), doi:[10.1029/2023JB026653](https://doi.org/10.1029/2023JB026653).

Heister, T., J. Dannberg, R. Gassmöller, and W. Bangerth (2017), High accuracy mantle convection simulation through modern numerical methods - II: Realistic models and problems, *Geophysical Journal International*, 210(2), 833–851, doi:[10.1093/gji/ggx195](https://doi.org/10.1093/gji/ggx195).

Hoggard, M. J., N. White, and D. Al-Attar (2016), Global dynamic topography observations reveal limited influence of large-scale mantle flow, *Nature Geoscience*, 9(6), 456–463, doi:[10.1038/ngeo2709](https://doi.org/10.1038/ngeo2709).

Hoggard, M. J., J. Winterbourne, K. Czarnota, and N. White (2017), Oceanic residual depth measurements, the plate cooling model, and global dynamic topography, *Journal of Geophysical Research: Solid Earth*, 122(3), 2328–2372, doi:[10.1002/2016JB013457](https://doi.org/10.1002/2016JB013457).

Hoggard, M. J., K. Czarnota, F. D. Richards, D. L. Huston, A. L. Jaques, and S. Ghelichkhan (2020a), Global distribution of sediment-hosted metals controlled by craton edge stability, *Nature Geoscience*, 13(7), 504–510, doi:[10.1038/s41561-020-0593-2](https://doi.org/10.1038/s41561-020-0593-2).

Hoggard, M. J., R. Parnell-Turner, and N. White (2020b), Hotspots and mantle plumes revisited: Towards reconciling the mantle heat transfer discrepancy, *Earth and Planetary Science Letters*, 542, doi:[10.1016/j.epsl.2020.116317](https://doi.org/10.1016/j.epsl.2020.116317).

Holdt, M. C., N. J. White, S. N. Stephenson, and B. W. Conway-Jones (2022), Densely Sampled Global Dynamic Topographic Observations and Their Significance, *Journal of Geophysical Research: Solid Earth*, 127(7), e2022JB024,391, doi:[10.1029/2022JB024391](https://doi.org/10.1029/2022JB024391).

Kronbichler, M., T. Heister, and W. Bangerth (2012), High accuracy mantle convection simulation through modern numerical methods, *Geophysical Journal International*, 191(1), 12–29, doi:[10.1111/j.1365-246X.2012.05609.x](https://doi.org/10.1111/j.1365-246X.2012.05609.x).

Le Brocq, A. M., A. J. Payne, and A. Vieli (2010), An improved Antarctic dataset for high resolution numerical ice sheet models (ALBMAP v1), *Earth System Science Data*, 2(2), 247–260, doi:[10.5194/essd-2-247-2010](https://doi.org/10.5194/essd-2-247-2010).

Lloyd, A. J., D. A. Wiens, H. Zhu, J. Tromp, A. A. Nyblade, R. C. Aster, S. E. Hansen, I. W. D. Dalziel, T. J. Wilson, E. R. Ivins, and J. P. O'Donnell (2020), Seismic Structure of the Antarctic Upper Mantle Imaged with Adjoint Tomography, *Journal of Geophysical Research: Solid Earth*, 125(3), 2019JB017,823, doi:[10.1029/2019JB017823](https://doi.org/10.1029/2019JB017823).

Martin, M. A., R. Winkelmann, M. Haseloff, T. Albrecht, E. Bueler, C. Khroulev, and A. Levermann (2011), The Potsdam Parallel Ice Sheet Model (PISM-PIK) – Part 2: Dynamic equilibrium simulation of the Antarctic ice sheet, *The Cryosphere*, 5(3), 727–740, doi:[10.5194/tc-5-727-2011](https://doi.org/10.5194/tc-5-727-2011).

Matthews, S., O. Shorttle, and J. MacLennan (2016), The temperature of the Icelandic mantle from olivine-spinel aluminum exchange thermometry, *Geochemistry, Geophysics, Geosystems*, 17(11), 4725–4752, doi:[10.1002/2016GC006497](https://doi.org/10.1002/2016GC006497).

Mitrovica, J. X., J. Austermann, S. Coulson, J. R. Creveling, M. J. Hoggard, G. T. Jarvis, and F. D. Richards (2020), Dynamic Topography and Ice Age Paleoclimate, *Annual Review of Earth and Planetary Sciences*, 48(1), 585–621, doi:[10.1146/annurev-earth-082517-010225](https://doi.org/10.1146/annurev-earth-082517-010225).

Moucha, R., A. M. Forte, J. X. Mitrovica, D. B. Rowley, S. Quéré, N. A. Simmons, and S. P. Grand (2008), Dynamic topography and long-term sea-level variations: There is no such thing as a stable continental platform, *Earth and Planetary Science Letters*, 271(1-4), 101–108, doi:[10.1016/j.epsl.2008.03.056](https://doi.org/10.1016/j.epsl.2008.03.056).

NOAA National Centers for Environmental Information (2022), ETOPO 2022 15 Arc-Second Global Relief Model, doi:[10.25921/FD45-GT74](https://doi.org/10.25921/FD45-GT74).

Paxman, G., J. Austermann, and A. Hollyday (2022), Grid files of the total isostatic response to the complete unloading of the Greenland and Antarctic Ice Sheets (version 1), doi:[10.18739/A2280509Z](https://doi.org/10.18739/A2280509Z).

Paxman, G. J. G. (2023), Antarctic palaeotopography, *Geological Society, London, Memoirs*, 56(1), 231–251, doi:[10.1144/M56-2020-7](https://doi.org/10.1144/M56-2020-7).

Paxman, G. J. G., E. G. W. Gasson, S. S. R. Jamieson, M. J. Bentley, and F. Ferraccioli (2020), Long-Term Increase in Antarctic Ice Sheet Vulnerability Driven by Bed Topography Evolution, *Geophysical Research Letters*, 47(20), e2020GL090,003, doi:[10.1029/2020GL090003](https://doi.org/10.1029/2020GL090003).

Poore, H. R., N. White, and S. Jones (2009), A Neogene chronology of Iceland plume activity from V-shaped ridges, *Earth and Planetary Science Letters*, 283(1-4), 1–13, doi:[10.1016/j.epsl.2009.02.028](https://doi.org/10.1016/j.epsl.2009.02.028).

Richards, F. D., M. J. Hoggard, N. White, and S. Ghelichkhan (2020), Quantifying the Relationship Between Short-Wavelength Dynamic Topography and Thermomechanical Structure of the Upper Mantle Using Calibrated Parameterization of Anelasticity, *Journal of Geophysical Research: Solid Earth*, 125(9), doi:[10.1029/2019JB019062](https://doi.org/10.1029/2019JB019062).

Richards, F. D., S. L. Coulson, M. J. Hoggard, J. Austermann, B. Dyer, and J. X. Mitrovica (2023a), Geodynamically corrected Pliocene shoreline elevations in Australia consistent with midrange projections of Antarctic ice loss, *Tech. rep.*

Richards, F. D., M. J. Hoggard, S. Ghelichkhan, P. Koelemeijer, and H. C. P. Lau (2023b), Geodynamic, geodetic, and seismic constraints favour deflated and dense-cored LLVPs, *Earth and Planetary Science Letters*, 602, 117,964, doi:[10.1016/j.epsl.2022.117964](https://doi.org/10.1016/j.epsl.2022.117964).

Ritsema, J., A. Deuss, H. J. van Heijst, and J. H. Woodhouse (2011), S40RTS: a degree-40 shear-velocity model for the mantle from new Rayleigh wave dispersion, teleseismic traveltimes and normal-mode splitting function measurements, *Geophysical Journal International*, 184(3), 1223–1236, doi:[10.1111/j.1365-246X.2010.04884.x](https://doi.org/10.1111/j.1365-246X.2010.04884.x).

Schaeffer, A. J., and S. Lebedev (2013), Global shear speed structure of the upper mantle and transition zone, *Geophysical Journal International*, 194(1), 417–449, doi:[10.1093/gji/ggt095](https://doi.org/10.1093/gji/ggt095).

Seton, M., R. Müller, S. Zahirovic, C. Gaina, T. Torsvik, G. Shephard, A. Talsma, M. Gurnis, M. Turner, S. Maus, and M. Chandler (2012), Global continental and ocean basin reconstructions since 200Ma, *Earth-Science Reviews*, 113(3-4), 212–270, doi:[10.1016/j.earscirev.2012.03.002](https://doi.org/10.1016/j.earscirev.2012.03.002).

Shorttle, O., J. MacLennan, and S. Lambart (2014), Quantifying lithological variability in the mantle, *Earth and Planetary Science Letters*, 395, 24–40, doi:[10.1016/j.epsl.2014.03.040](https://doi.org/10.1016/j.epsl.2014.03.040).

Simmons, N. A., A. M. Forte, and S. P. Grand (2009), Joint seismic, geodynamic and mineral physical constraints on three-dimensional mantle heterogeneity: Implications for the relative importance of thermal versus compositional heterogeneity, *Geophysical Journal International*, 177(3), 1284–1304, doi:[10.1111/j.1365-246X.2009.04133.x](https://doi.org/10.1111/j.1365-246X.2009.04133.x).

Simmons, N. A., S. C. Myers, G. Johannesson, E. Matzel, and S. P. Grand (2015), Evidence for long-lived subduction of an ancient tectonic plate beneath the southern Indian Ocean, *Geophysical Research Letters*, 42(21), 9270–9278, doi:[10.1002/2015GL066237](https://doi.org/10.1002/2015GL066237).

Steinberger, B., S. C. Werner, and T. H. Torsvik (2010), Deep versus shallow origin of gravity anomalies, topography and volcanism on Earth, Venus and Mars, *Icarus*, 207(2), 564–577, doi:[10.1016/j.icarus.2009.12.025](https://doi.org/10.1016/j.icarus.2009.12.025).

Sutherland, R., S. Spasojevic, and M. Gurnis (2010), Mantle upwelling after Gondwana subduction death explains anomalous topography and subsidence histories of eastern New Zealand and West Antarctica, *Geology*, 38(2), 155–158, doi:[10.1130/G30613.1](https://doi.org/10.1130/G30613.1).

Wieczorek, M. A., and M. Meschede (2018), SHTools: Tools for Working with Spherical Harmonics, *Geochemistry, Geophysics, Geosystems*, 19(8), 2574–2592, doi:[10.1029/2018GC007529](https://doi.org/10.1029/2018GC007529).

Winkelmann, R., M. A. Martin, M. Haseloff, T. Albrecht, E. Bueler, C. Khroulev, and A. Levermann (2011), The Potsdam Parallel Ice Sheet Model (PISM-PIK) – Part 1: Model description, *The Cryosphere*, 5(3), 715–726, doi:[10.5194/tc-5-715-2011](https://doi.org/10.5194/tc-5-715-2011).

Wobbe, F., A. Lindeque, and K. Gohl (2014), Anomalous South Pacific lithosphere dynamics derived from new total sediment thickness estimates off the West Antarctic margin, *Global and Planetary Change*, 123(PA), 139–149, doi:[10.1016/j.gloplacha.2014.09.006](https://doi.org/10.1016/j.gloplacha.2014.09.006).

Yamauchi, H., and Y. Takei (2016), Polycrystal anelasticity at near-solidus temperatures, *Journal of Geophysical Research: Solid Earth*, 121(11), 7790–7820, doi:[10.1002/2016JB013316](https://doi.org/10.1002/2016JB013316).

A Appendices

A.1 Appendix A: Detailed Methods / Discussion

A.1.1 Antarctic DT-RT Mismatch

This section provides more detail on the Antarctic DT-RT mismatches discussed in Section 2.3.

The mismatch between DT and RT in the Amundsen Sea region of Antarctica may result from a lack of a correction for flexural impacts of large sediment loads in the RT data. [Hoggard et al. \(2017\)](#) demonstrates how flexure from a sedimentary load impacts the area's isostatic signature, with anomalies primarily occurring at load edges, whilst central areas and those further away are relatively unaffected. In their RT dataset, they acknowledge that this effect is not taken into account when calculating isostatic corrections, but they spatially average residual depths in 1° , 2° , and 4° bins, noting that flexural wavelengths are typically much shorter than the wavelength of DT so its effect should therefore be smoothed out. Antarctic sedimentary data from [Wobbe et al. \(2014\)](#) shows a 4 km thick sedimentary pile at this location. RT measurements lie exactly on the edge of this pile, whilst other measurements lie either on top of, or far away from, other piles. Furthermore, [Wobbe et al. \(2014\)](#) calculates residual basement depths, correcting for sedimentary loading, and finds values ranging 0.5 - 2.0 km, which would match DT predictions, further evidencing that the mismatch arises from a lack of sedimentary flexural loading corrections.

A.1.2 Temperature Models Merging Methodology

This section provides greater detail on the merging methods used to combine ANT-20 and SLNAAFSA into one temperature model, described in Section 3.1.1

Code, designed to merge seismic tomographic models, from S. Adourian ([Adourian and Frost, 2022](#)) was used to merge the respective tomographic models' temperature models. This methodology merges regional and global models by applying a mask in spherical harmonic space, which tapers the contribution of the regional model to 0 at its boundary, creating a smooth transition into the global background model. Representing a mask defining ANT-20's extent (regional model) in spherical harmonics using the pyshtools Python package([Wieczorek and Meschede, 2018](#)), smooths the mask into a taper at its boundaries. This mask is applied to the regional model and summed with the global model. To minimise spectral ringing artefacts, the model is expressed up to a lower spherical harmonic degree ($l\text{-max}_{\text{eff}}$) than it is expanded to ($l\text{-max}$). The method was originally developed for seismic velocity model merging, and therefore expects inputs to be expressed as an anomaly relative to a 1D average. 1D temperature averages were therefore calculated and subtracted from both models before merging.

Initially, an issue was noted in the merged results, with output temperatures in Antarctica approximately double those defined in ANT-20. The spherical harmonic components of the tapered regional model were being summed with those of the full global model, essentially representing a simple addition of ANT-20 and SLNAAFSA values. This approach is a sensible choice when—as in the original example the method was developed for—the regional model is dominantly composed of short wavelengths and the global model mostly comprises long wavelengths. In such a case, when the two are summed in frequency space, the regional model fills gaps in the short-wavelength band of the global model power spectrum, and overall spectral amplitudes match those of the original datasets. However, in my case, there is substantial overlap in the spherical harmonic power spectra of the SLNAAFSA and ANT-20 models since they are both composed of long and short wavelengths. As a result, this simplistic summation approach produces artificially large spectral amplitudes and unreasonably high temperatures within the region of ANT-20.

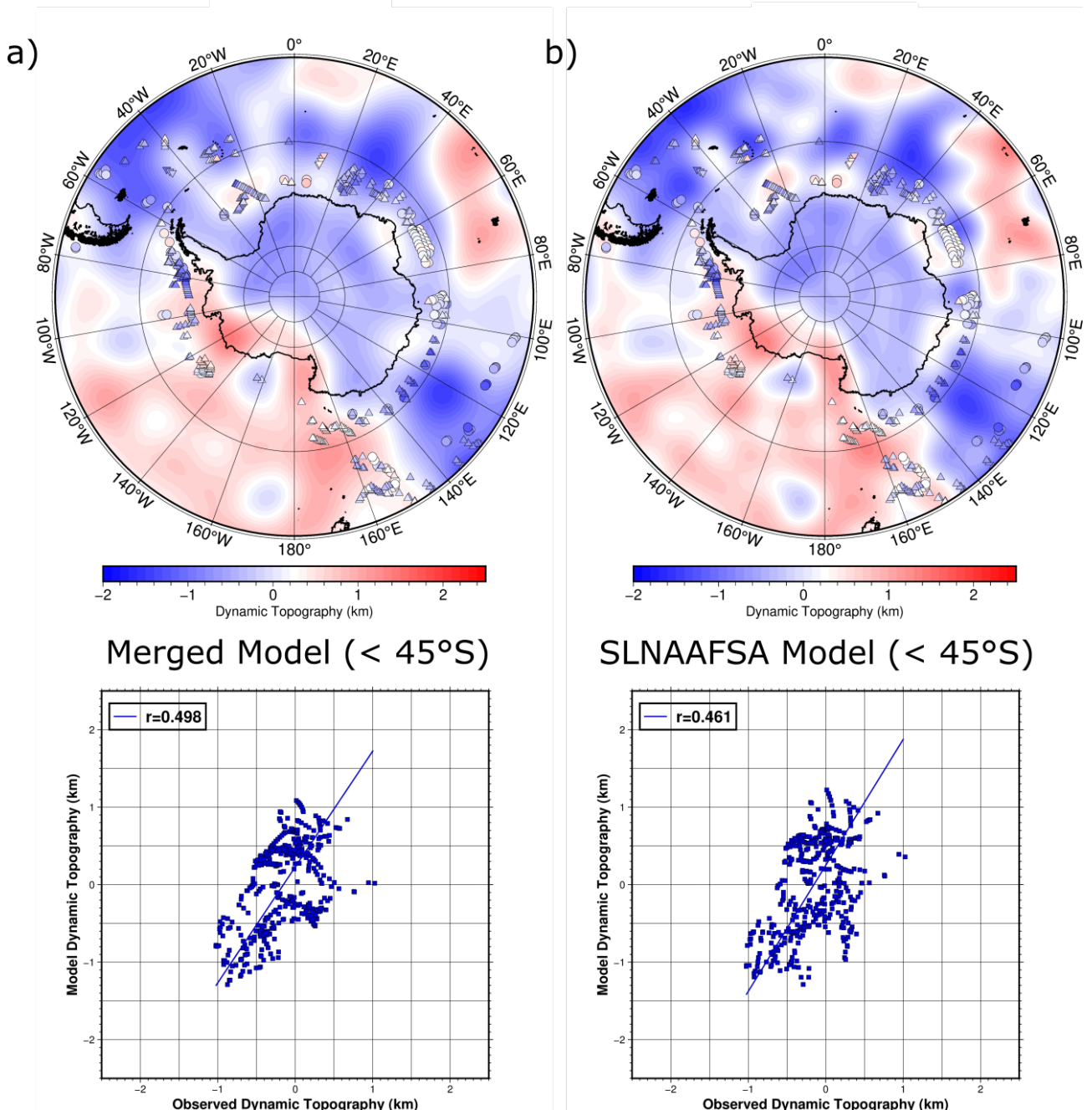


Figure 19: Maps showing *Hoggard et al.* (2017) observed residual topography data over present-day dynamic topography models generated from this study's merged model (S40RTS lower-mantle model (*Ritsema et al.*, 2011)) for all latitudes $< 45^{\circ}$ S. Bottom panels show data distribution, line of best fit and Pearson's correlation coefficient. **a)** shows results of the merged model, incorporating SLNAAFSA and ANT-20 in the upper mantle (*Hoggard et al.*, 2020a; *Lloyd et al.*, 2020). **b)** shows equivalent model incorporating only SLNAAFSA.

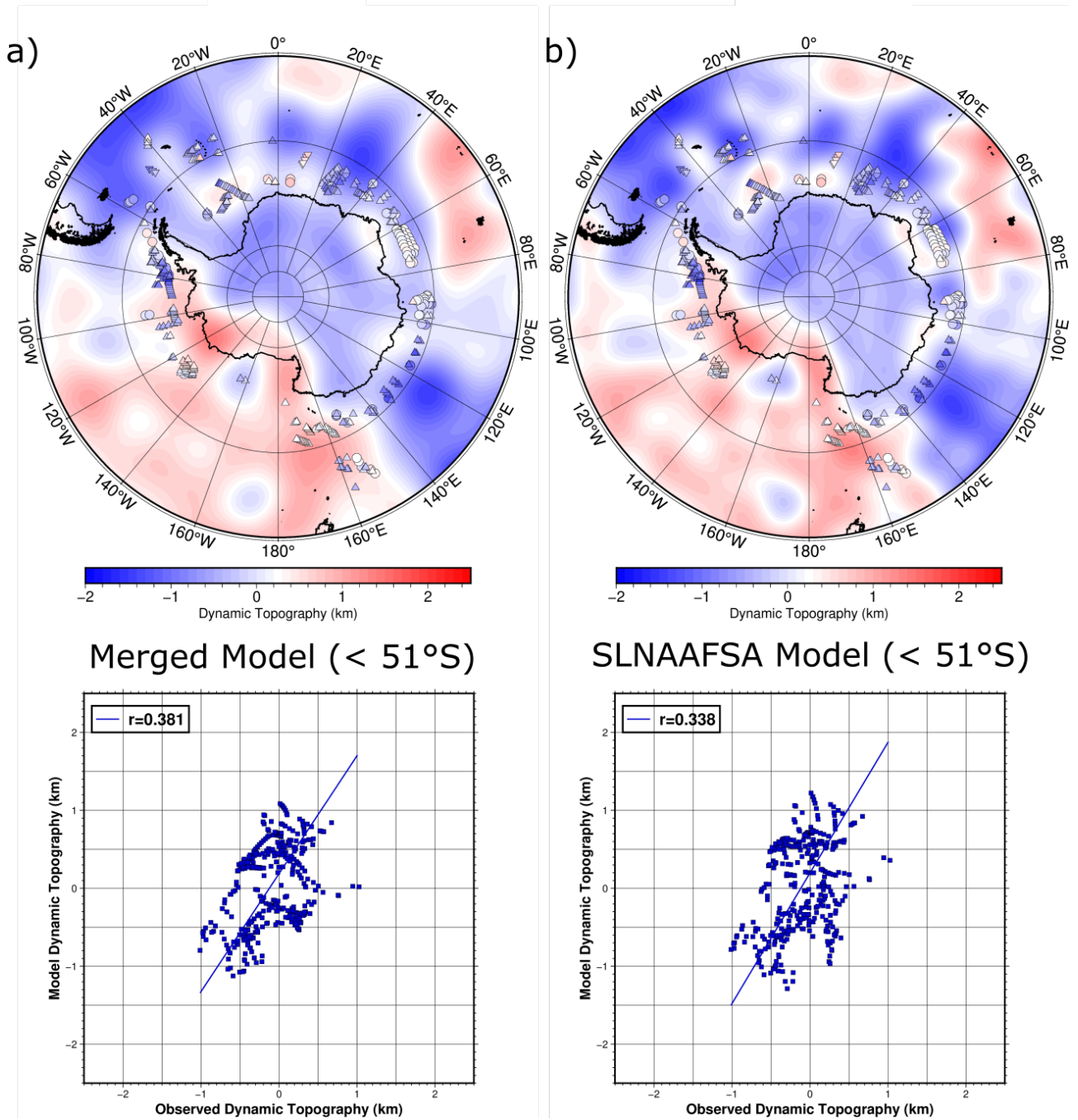


Figure 20: Maps showing *Hoggard et al.* (2017) observed residual topography data over present-day dynamic topography models generated from this study's merged model (S40RTS lower-mantle model (*Ritsema et al.*, 2011)) for all latitudes < 51°S (excluding ANT-20 to SLNAAFSA transition zone). Bottom panels show data distribution, line of best fit and Pearson's correlation coefficient. **a)** shows results of the merged model, incorporating SLNAAFSA and ANT-20 in the upper mantle (*Hoggard et al.*, 2020a; *Lloyd et al.*, 2020). **b)** shows equivalent model incorporating only SLNAAFSA.

To avoid this undesirable amplitude inflation, the code was edited to create an 'inverse taper', in the opposite direction to the main taper, that would be applied to the global grid up to a certain latitude, in this case 51°S. The regional mask is also defined to taper between its border, 45°S, and this limit. Thus, when summed, an effective average of both grids is made in this transition region, with contributions of both grids tapering to 0 in opposite directions. Above 45°S, the model is purely SLNAAFSA, with no ANT-20 contribution, and vice-versa below 51°S.

A.1.3 Merged Model Present-day Dynamic Topography

This section discusses correlations between this study's present-day predicted DT and RT data, briefly mentioned in Section 3.2. Following [Richards et al. \(2023b\)](#), present-day DT models were created to assess the degree to which the merged model improves agreement with independent RT observations compared with an SLNAAFSA-only model. These outputs are generated using the instantaneous flow methodology described in Section 2.1.1.

Correlations between present-day dynamic topography from the merged model within the region of ANT-20 and [Hoggard et al. \(2017\)](#) RT data (Figure 19) indicate the inclusion of ANT-20 tomography improves fit with observed data compared to an SLNAAFSA-only model, though only by a small amount, with a 0.038 increase in correlation coefficient. However, when the region is restricted to exclude the transition zone created in the merging process (< 51°S, Figure 20), the correlation advantage of the ANT-20-inclusive merged model over the SLNAAFSA-only model widens to 0.043. Whilst this is, once again, a very small increase, it does imply that predicted DT becomes increasingly accurate closer to the Antarctic ice sheet when ANT-20 structure is included. Whilst absolute correlations do decrease, it is important to note that data-points within the excluded region are not evenly distributed, and disproportionately lie in well correlated areas, hence somewhat bias the correlations when included.

A.2 Appendix B: Extra Models

A.2.1 Extra Dynamic Topography and Residual Topography Datasets

DT–RT correlations, as discussed in Section 2.1.1, were also performed using RT data from [Holdt et al. \(2022\)](#) and predicted DT data from [Richards et al. \(2023a\)](#), which was generated following the same method as in Section 3. In general, the results of these supplementary comparisons differ little from the primary results discussed in the main text. [Holdt et al. \(2022\)](#) vs [Richards et al. \(2023b\)](#) has notably better correlations in Antarctica than other comparisons, however all show that Antarctic correlations are systematically worse than Greenland correlations, justifying the incorporation of ANT-20 in this region. Also evident in all dataset combinations is the Greenland offset of ~ 0.8 km, demonstrating that this is a real feature of North Atlantic residual topography and not simply an artefact affecting a single dataset.

A.2.2 Extra Ice Sheet Models

Ice-sheet models, discussed in Section 4, were also run for different parameterisations and models (Figures 22, 23), including fixing the bed to have no viscoelastic response to ice load changes, using a GPlates-based plate motions model ([Seton et al., 2012](#)), using the LLNL-G3D-JPS (S15) lower-mantle model ([Simmons et al., 2015](#)) and testing an SLNAAFSA-only model for the upper mantle, with no incorporation of ANT-20 ([Hoggard et al., 2020a; Richards et al., 2020; Lloyd et al., 2020](#)). A test was also run to set viscoelastic starting parameters to current GIA rates, since it is unlikely the bed was in perfect isostatic equilibrium at the time. However, these provided no change to the results, hence were not included. Fixed-bed scenarios resulted

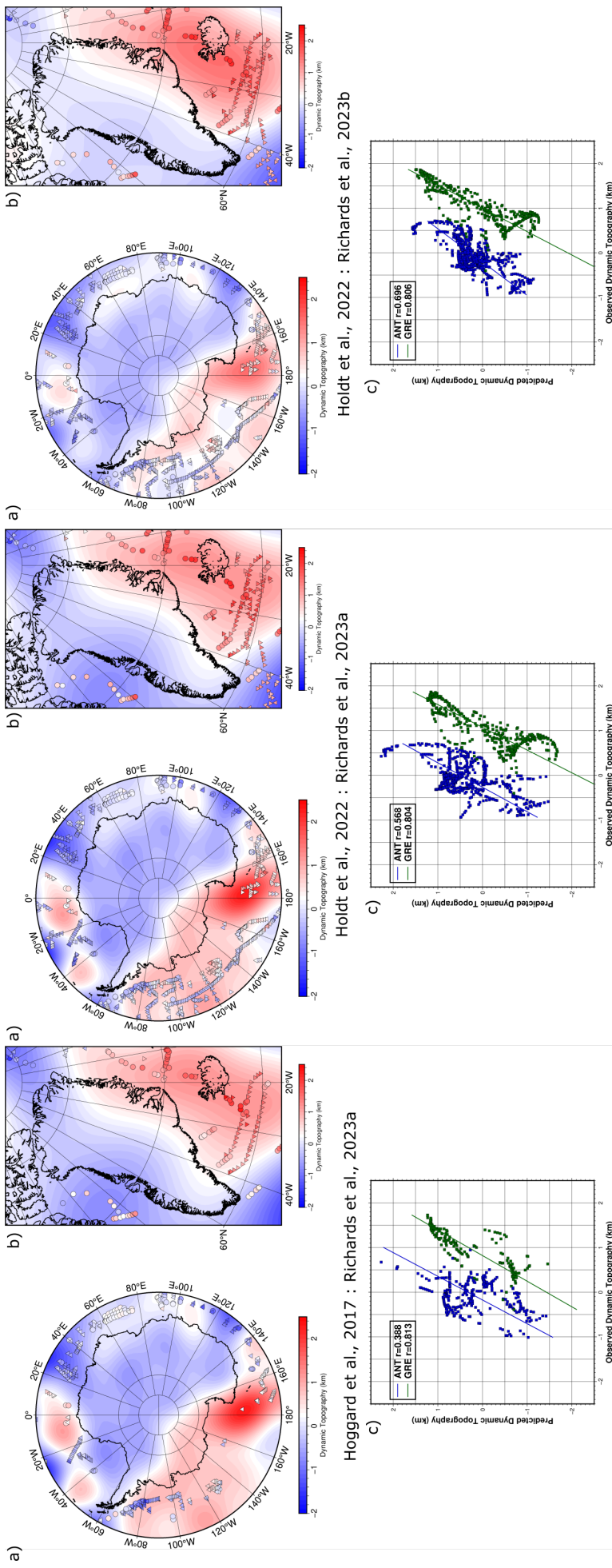


Figure 21: a), b) Map of Antarctica, Greenland respectively. Grid data is predicted present-day DT from [Richards et al. \(2023a\)](#). Point data (circles, triangles) are RT measurements from [Hoggard et al. \(2017\)](#). Circles represent data-points corrected for both sediment and crustal thickness, triangles only only corrected for sediment thickness, representing upper and lower bounds, following the symbol style of [Hoggard et al. \(2017\)](#). Both the residual and dynamic topography data are plotted with the same colour-scheme. c) Plot of model dynamic topography vs observed residual topography. Antarctic data points in blue, Greenland data points in green, with Pearson's correlation coefficient, r , displayed in legend. d), e), f) Equivalent plots using RT data from [Holdt et al. \(2022\)](#) and predicted DT from [Richards et al. \(2023b\)](#).

in the most extreme differences between modern and MPWP equilibrium ice volumes, with more widespread, significant changes in ice thickness in West Antarctica (± 4000 m), although the spatial distribution of losses and gains remain the same. Results for GPlates motions, S15 lower-mantle and SLNAAFSA-only runs all had similar outcomes, with complete ice loss in the Ross Sea as before, and some ice gain at the Ronne Ice Shelf.

Timeseries plots of each run (Figures 24, 25) display the evolution of ice volume towards dynamic equilibrium as it is spun up over 100 kyr. The most dramatic change in ice volume, and SLE, once again comes from the fixed bed scenarios, with 4.2 m of Pliocene sea-level rise attributable to changes in DT. This is expected to exaggerate the impacts of DT change as it unrealistically does not consider viscoelastic rebound of the bedrock in regions where the ice thins, a process that helps to restabilise the ice-sheet. Notably, the SLNAAFSA-only run, which used identical parameters to the primary run, but does not include ANT-20-derived mantle structure, resulted in 0.5 m less of GMSL rise attributable to DT changes, indicating that incorporation of the higher-resolution regional model does have a significant impact on predicted equilibrium ice volume.

Greenland ice sheet thickness, volume and SLE saw little to no change over its three parameterisations, showing that DT is a significantly less important factor in the evolution of the GIS since the MPWP.

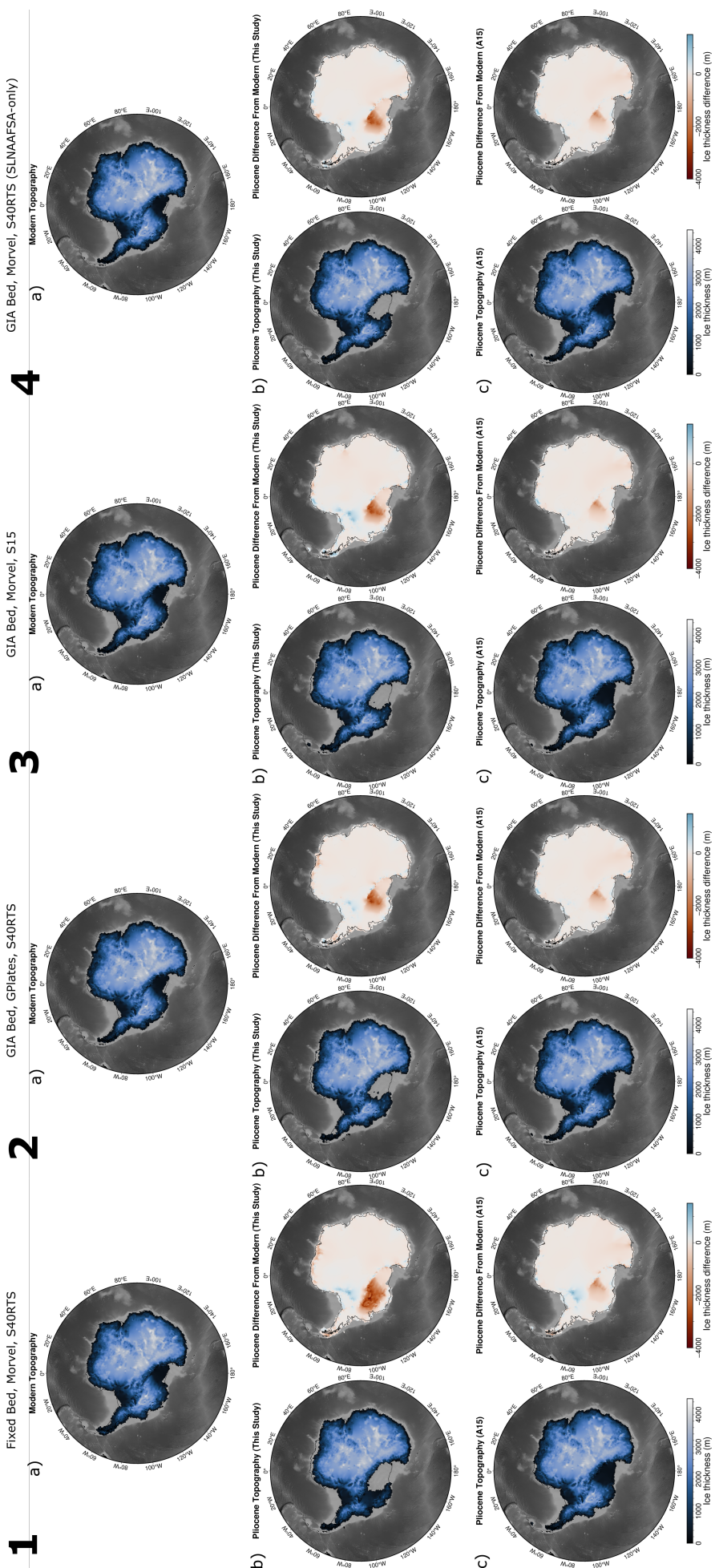


Figure 22: Maps of Antarctic ice thickness for MPWP reference model. Background topography is ETOPO bedrock data from NOAA National Centers for Environmental Information (2022). **a)** Modern topography ice-sheet model. **b)** Left: Pliocene-corrected topography ice-sheet model. Right: Difference of Pliocene ice-thickness from modern. **c)** Ice-sheet model from Austermann *et al.* (2015) (A15). Left: Pliocene Ice thickness. Right: Pliocene ice-thickness difference from modern. **1.** Fixed bed (no viscoelastic response), Morvel plate motions (DeMets *et al.*, 2010), S40RTS lower-mantle model (Ritsema *et al.*, 2011) **2.** GPPlates plate model (Seton *et al.*, 2012) and S40RTS lower-mantle model on a viscoelastically deforming bed. **3.** Morvel plate model and S15 lower-mantle model (Simmons *et al.*, 2015) on a viscoelastically deforming bed using only SLNAAFS-A upper-mantle model (no ANT-20 incorporated) (Hoggard *et al.*, 2020a; Richards *et al.*, 2020; Lloyd *et al.*, 2020)..

1 Fixed Bed, Morvel, S40RTS

2 GIA Bed, GPlates, S40RTS

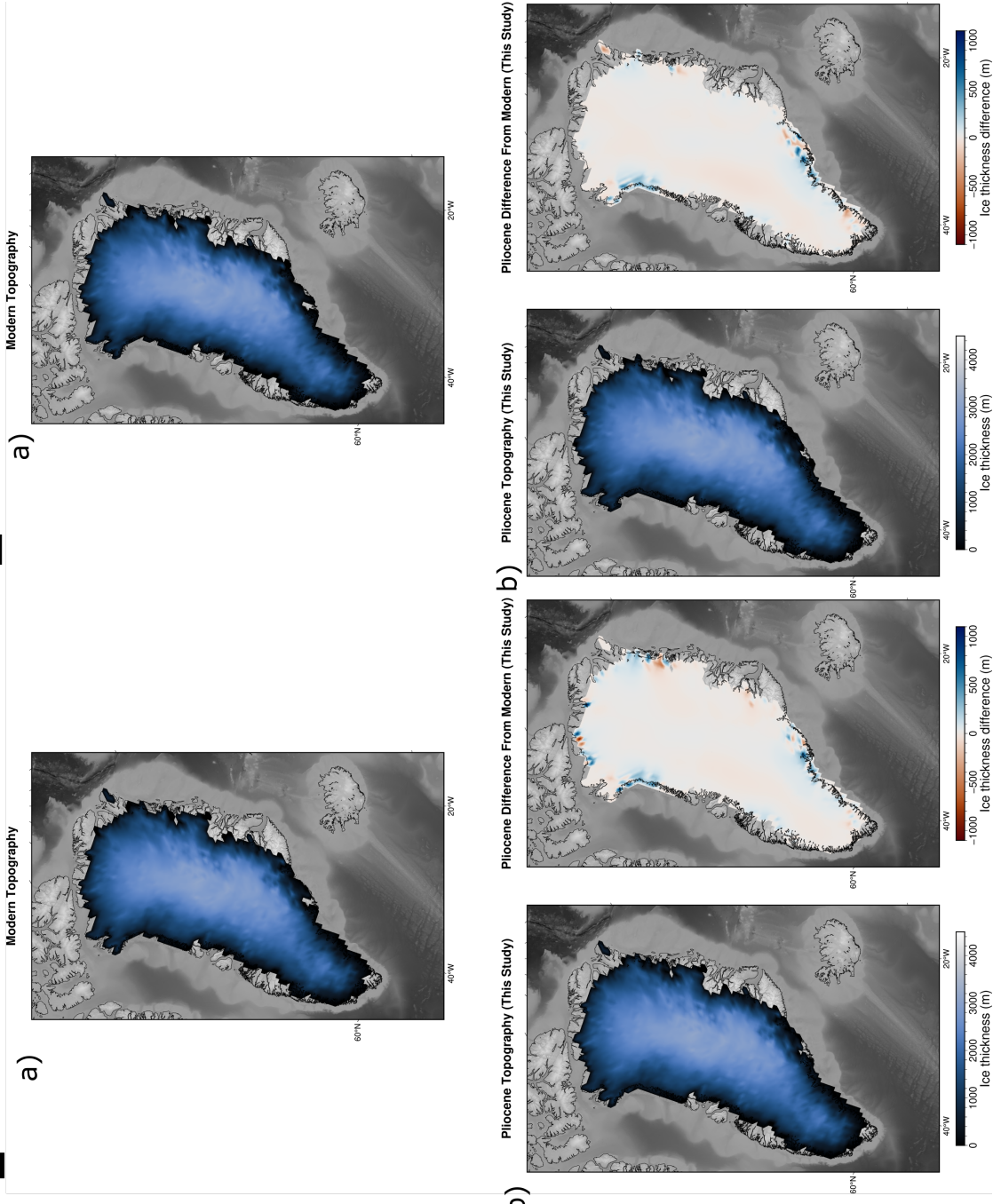


Figure 23: Maps of Greenland ice thickness for MPWP reference model. Background topography is ETOP0 bedrock data from NOAA National Centers for Environmental Information (2022). **a)** Modern topography and Pliocene Topography (This Study) for both Fixed bed (no viscoelastic response) and GIA Bed, GPlates, S40RTS lower-mantle model. **b)** Difference of Pliocene ice-thickness from modern for both models.

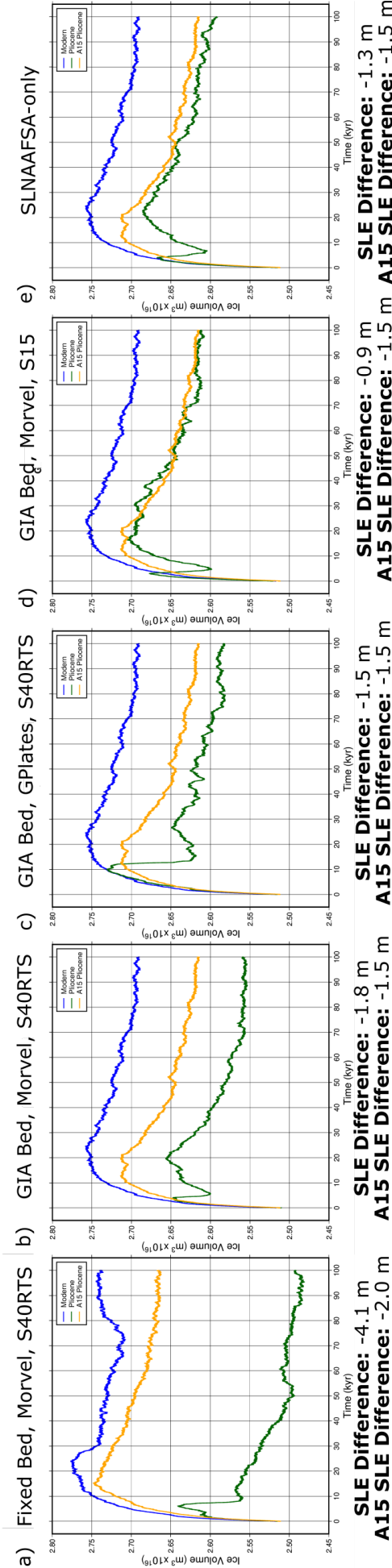


Figure 24: Plots showing the evolution of Antarctic ice volume in models with time as it heads towards equilibrium. Blue lines are runs on modern topography, green lines are run on Pliocene-corrected topography from this study, orange lines are run on Pliocene-corrected topography from *Austermann et al.* (2015) (A15). SLE difference is change in sea-level rise equivalent held in ice in MPWP the from modern model. **a)** Fixed bed (no viscoelastic response) using Morvel plate motions (*DeMets et al.*, 2010) and S40RTS lower-mantle model (*Ritsma et al.*, 2011). **b)** GIA bed (including viscoelastic response) using Morvel plate motions and S40RTS lower-mantle model. **c)** GIA bed (including viscoelastic response) using GPIates plate motions *Seton et al.* (2012) and S40RTS lower-mantle model. **d)** GIA bed (including viscoelastic response) using Morvel plate motions and S15 lower-mantle model (*Simmons et al.*, 2015). **e)** GIA bed (including viscoelastic response) using Morvel plate motions and S40RTS lower-mantle model, using SLNAAFFSA-only upper-mantle (no ANT-20 incorporated) (*Hoggard et al.*, 2020a; *Richards et al.*, 2020; *Lloyd et al.*, 2020).

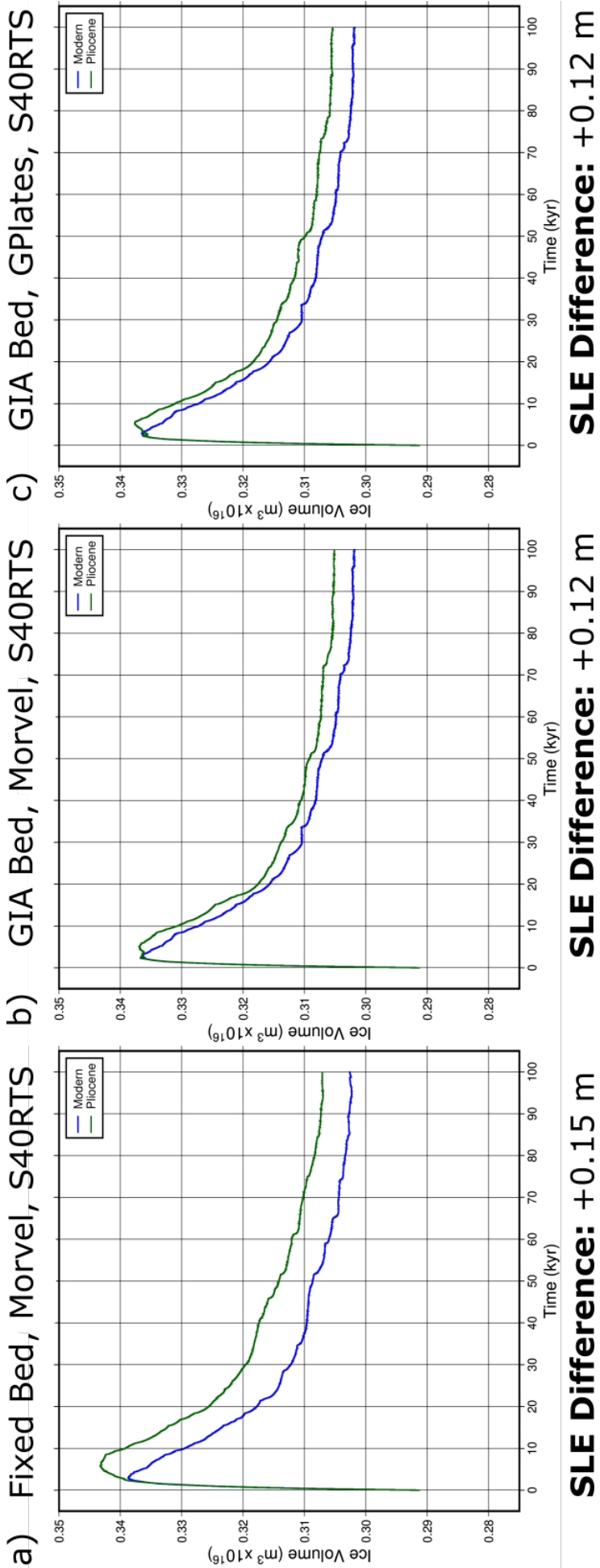


Figure 25: Plots showing the evolution of Greenland ice volume in models with time as it heads towards equilibrium. Blue lines are runs on modern topography, green lines are run on Pliocene-corrected topography from this study. SLE difference is change in sea-level rise equivalent held in ice in MPWP from the modern model. a) Fixed bed (no viscoelastic response) using Morvel plate motions (*DeMets et al.*, 2010) and S40RTS lower-mantle model (*Ritsema et al.*, 2011). b) GIA bed (including viscoelastic response) using Morvel plate motions and S40RTS lower-mantle model. c) GIA bed (including viscoelastic response) using GPIates plate motions *Seton et al.* (2012) and S40RTS lower-mantle model.